CHARACTERIZING DEFORMATION ALONG AN EARLY-STAGE RIFT: GPS OBSERVATIONS FROM THE NORTHERN LAKE MALAWI (NYASA) RIFT

by

Grant Bonnette

A Thesis

Submitted to the Faculty of Purdue University

In Partial Fulfillment of the Requirements for the degree of

Master of Science

Department of Earth, Atmospheric, and Planetary Sciences

West Lafayette, Indiana

May 2020

THE PURDUE UNIVERSITY GRADUATE SCHOOL
STATEMENT OF COMMITTEE APPROVAL

Dr. Julie Elliott, Chair

Department of Earth, Atmospheric, and Planetary Sciences

Dr. Christopher Andronicos

Department of Earth, Atmospheric, and Planetary Sciences

Dr. Lucy Flesch

Department of Earth, Atmospheric, and Planetary Sciences

Dr. Matt Pritchard

Department of Earth and Atmospheric Sciences

Cornell University

Approved by:

Dr. Christopher Andronicos

To my parents, who never stopped believing in me.

ACKNOWLEDGMENTS

Foremost, I must thank my advisor Julie Elliott for her unending patience and support during my time at Purdue. Without her guidance, this project would not have been possible. I am indebted to my committee members, Dr. Christopher Andronicos, Dr. Lucy Flesch, and Dr. Matt Pritchard for their continued support of my project and their constructive feedback throughout this process. I would like to thank the National Science Foundation and Columbia University for support of this work under grant EAR-1110921. I am grateful for the constructive feedback members of the SEGMeNT project provided at AGU 2018. I would also like to thank the Department, countless faculty, and staff who have helped me achieve my goals at Purdue. Finally, I would like to thank my family and friends for providing unfailing support throughout this process.

TABLE OF CONTENTS

LIST OF TABLES

LIST OF FIGURES

ABSTRACT

The Malawi (Nyasa) Rift is a prominent example of immature rifting located along the southern East African Rift System. The SEGMeNT (Study of Extension and maGmatism in Malawi aNd Tanzania) project installed a new network of 12 continuous GPS sites in Malawi, Tanzania, and Zambia. Using this new data along with data from other existing sites in the region, I examine the present-day deformation along the Malawi Rift and surrounding areas. The GPS data is used to constrain a tectonic block model of the Malawi Rift in order to produce estimates of angular velocities of the blocks, which are then used to derive fault slip rates and linear block velocities. The new data around the Malawi Rift suggests an additional block may be required to explain the observed deformation. My preferred model predicts that extension rates in the area are slower than previous studies suggested (3.8 ± 0.7 mm/yr; Stamps et al., 2008) with a cumulative rate 2.35 ± 0.65 mm/yr in the northern Malawi Rift and 1.26 ± 0.85 mm/yr along the southern Malawi Rift.

1. INTRODUCTION

The Malawi Rift is a 650km subset of the western branch of the East African Rift system, serving as the boundary between the Nubia plate and the Rovuma microplate. It is a prime example of immature rifting with discrete border faults, diffuse seismicity, and small amounts of volcanism. Rifting in this area has generated Lake Malawi (Figure 1), the second deepest lake in the East African Rift at 700m (Specht & Rosendahl, 1989), but the present-day kinematics associated with the rifting are not fully understood.

Several previous studies used geophysical techniques to shed light on various aspects of the kinematics. Saria et al., (2013) Saria et al., (2014), and Stamps et al., (2008) all used GPS geodesy to examine the East African Rift as a whole, but their data resolution was too broad to robustly determine kinematics at the scale of the Malawi rift. Specht & Rosendahl (1989) and Flannery & Rosendahl (1990) both analyzed seismic reflection data published as part of Project PROBE (Scholz et al., 1989), an offshore seismic reflection dataset covering Lake Malawi, to map the rift architecture. Rosendahl et al., (1992) further analyzed the seismic reflection data by examining fault systems to discuss sedimentation rates in Malawi and other African rift lakes. Mortimer et al., (2007) integrated Project PROBE data with shallow seismic data to improve mapping of regional faults. Shillington et al., (2016) collected new onshore and offshore multichannel seismic, magnetotelluric, GPS, and geochemical data, selections of which have been integrated into multiple studies (e.g. Accardo et al., 2017; Ebinger et al., 2019, Shillington et al., 2020) to further understand the rift architecture. Despite these attempts, there are still questions left unanswered concerning certain aspects of the deformation. Is the deformation localized? Does deformation align with the border faults? Do the border faults pose the major seismic hazards in the region? How does deformation happen in immature rifting?

As a part of the SEGMeNT (Study of Extension and maGmatism in Malawi aNd Tanzania) project, 12 new continuous GPS sites shown in Figure 1 were installed in northern Malawi, Tanzania, and Zambia. These new sites, combined with additional data from existing sites, will be used as inputs in a tectonic block model of the Malawi Rift. This kinematically self-consistent model, using the methods of Meade and Loveless (2009), combines GPS velocities with *a priori* fault slip rates and fault geometries to simultaneously estimate block motion and slip rates on faults.

Together, the improved localized GPS dataset and the block modeling technique will allow for an updated view of the present-day deformation of the Malawi Rift system.

a)

b)

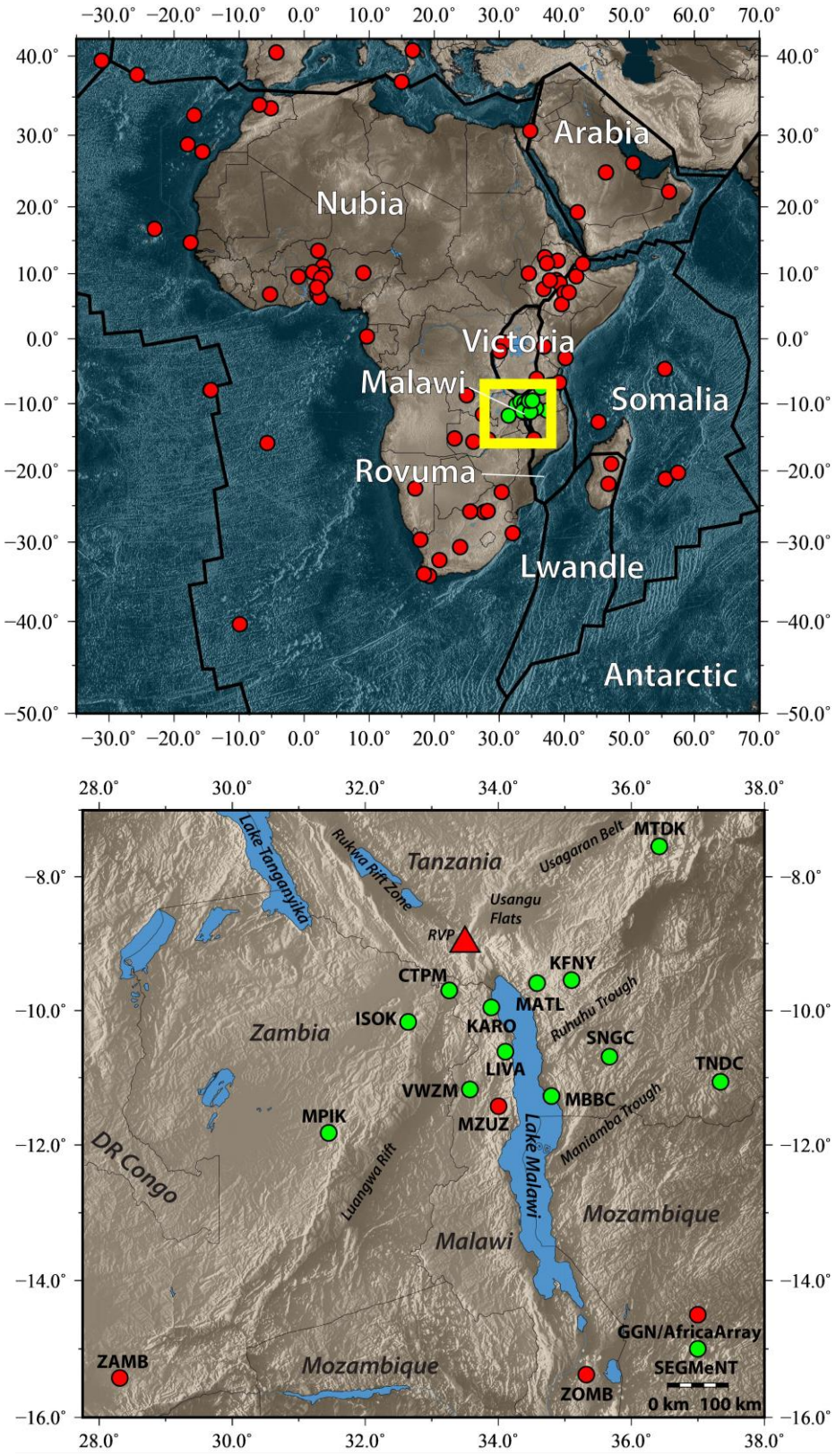

Figure 1 a) GPS sites on Nubia and other near field plates. Yellow bounding box is the extent of panel b. b) GPS Sites major features around Malawi. Red dots are GGN/AfricaArray/other sites. Green dots are SEGMeNT sites. RVP is the Rungwe Volcanic Province.

2. TECTONIC SETTING AND PREVIOUS WORK

The East African Rift is a prominent example of active rifting. Most likely initiated by a mantle plume (Ebinger & Sleep, 1998; Halldórsson et al., 2014), modern extension started in the Oligocene (Macgregor, 2015) in Ethiopia and Kenya. It then continued to propagate southward, eventually developing into the Eastern, Western, and Southeastern branches (Figure 2). The Eastern and Western branches differ significantly, with the Eastern branch having a larger thermal anomaly, increased amounts of volcanism, and a more mature rift as compared to the Western branch. The Western Branch is primarily amagmatic apart from the Virunga Complex around Lakes Kivu and Edward and the Rungwe volcanic complex north of Lake Malawi (Ebinger et al., 2019; Ebinger & Sleep, 1998; Macgregor, 2015). Along the Western Branch, the primarily N-S trending Malawi and Tanganyika Rifts accommodate the NW-SE extension by a complex transfer zone via the Rukwa Rift Basin (Chorowicz, 2005; Roberts et al., 2012). Traditionally, rifting requires upwelling of hot mantle material to weaken strong, thick lithosphere (Buck, 2004). However, the required heat flow (e.g. Njinju et al., 2019; O'Donnell et al., 2013; 2016) required to rupture the lithosphere in the western rift (Buck, 2004) does not seem to be present. These amagmatic endmembers of rifting suggest that traditional methods of calculating forces do not encompass the entire system; more work is needed to fully understand the processes.

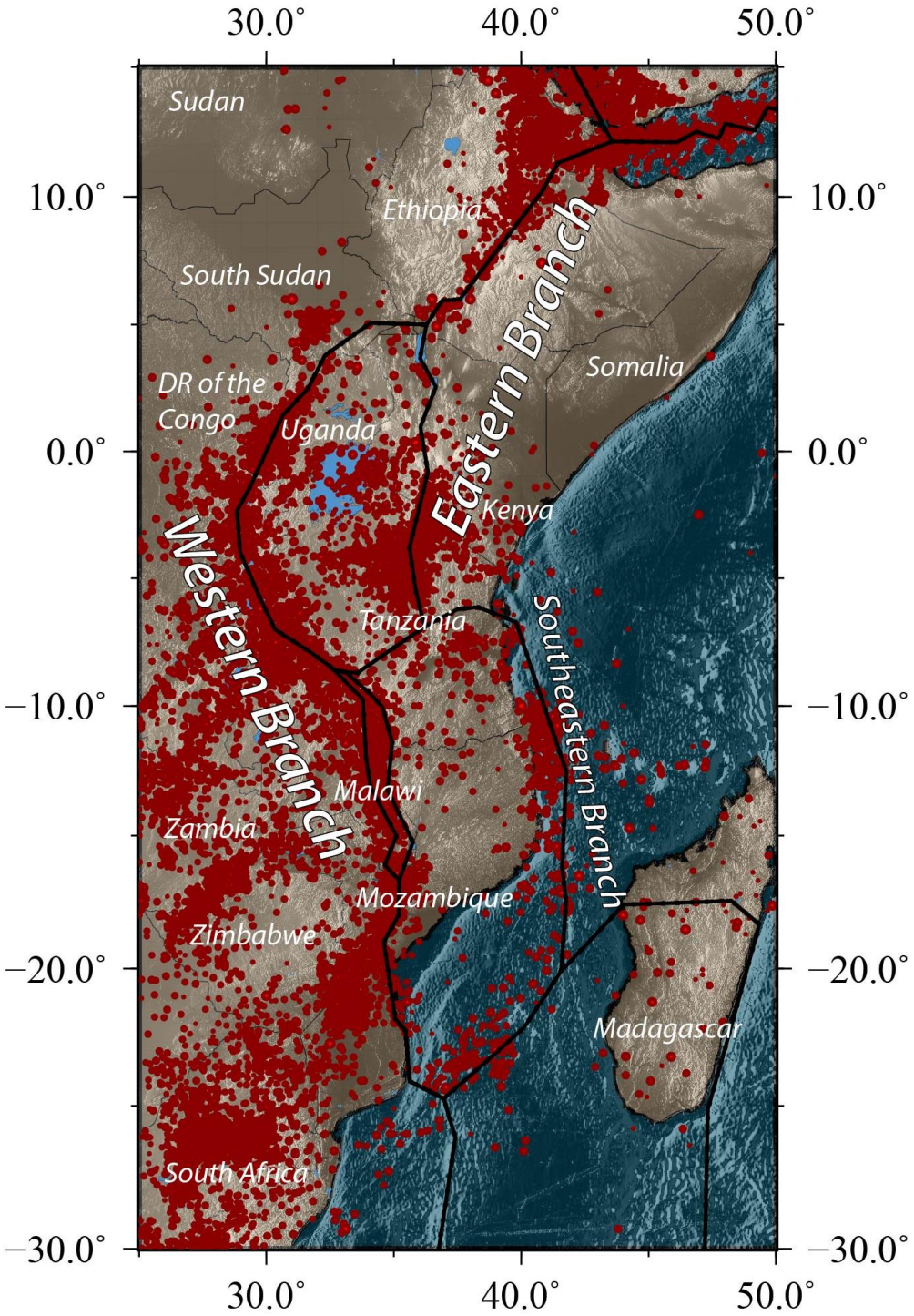

Figure 2 Eastern, Western, and Southeastern branches of the East African Rift plotted with seismicity and block boundaries from this model.

Located on the southern edge of the Western Branch, the Malawi Rift originated in the Miocene (Chorowicz, 2005; Macgregor, 2015; Roberts et al., 2012). Outcrop (Bromage et al., 1995; Ring & Betzler, 1995) and gravity (Ebinger et al., 1993) data suggest that major extension events have been occurring since 5 Ma (Macgregor, 2015) but these events have remained primarily amagmatic. The Malawi Rift itself is comprised of a series of alternating polarity, tilted half grabens that are bounded by large border faults. Between half grabens, intrabasin regions known as accommodation zones, are present to facilitate stress transfers via oblique slip faults (e.g. Ebinger, 1989a; Ebinger et al., 1987; Specht & Rosendahl, 1989).

Previous deformation events may be influencing the structure of the Cenozoic rifting. Two Precambrian deformation bands are located around Lake Malawi and could potentially provide a way to complicate deformation in the area by providing pre-existing structures that could reactivate (Kolawole et al., 2018). The western band, the Irumide, is a NE-SW trending band of igneous and metamorphic rocks that provides the basement fabric for the Malawi Rift. The northern band, the Ubendian, served as a fault zone to accommodate the strike slip motion across the Irumide belt (Daly, 1986). Both Precambrian belts may have created weak zones in the lithosphere that may be reactivating in the Cenozoic rifting events (Delvaux, 2001; McConnell, 1972). Reactivation of pre-existing structures may also be occurring in the Ruhuhu and Metangula basins east of Lake Malawi where Permian (Karoo) rifts provide weak zones (Delvaux, 2001; Ebinger et al., 1984; Kolawole et al., 2018).

The area around Lake Malawi is seismically active and has the potential to generate devastating earthquakes. In recent years, several significant $M_w > 5.0$ earthquakes have occurred (Hodge et al., 2015) (Figure 3). The 1989 Salima-Dedza-Mchinji earthquakes had multiple foreshocks southwest of Salima, Malawi, with the largest being a M_w 5.4 on March 9th, 1989. This was followed by the M_w 6.1 main shock a day later, causing intense shaking in Lilongwe, Malawi's capital city, with shaking felt into Mozambique and Zambia (Gupta & Malomo, 1995; Hodge et al., 2015). The Karonga earthquake swarm from December 6-19, 2009 produced four earthquakes with a $M_w > 5.0$ (Biggs et al., 2010). These quakes severely impacted locals, displacing over 30,000 people and being felt by over 200,000 people (Office of the United Nations Resident Coordinator, 2009). Although none have been measured, larger earthquakes with $M_w > 7.0$ may be possible (Biggs et al., 2010; Hodge et al., 2015) on multiple faults based on the length of the rupture, thickness of the crust, seismic moment, and plate motion. However, the recurrence interval for

many of these faults is calculated to be on the order of thousands of years. Some fault systems (e.g. Livingstone) may be capable of producing earthquakes with M_w ~8.0, but with much smaller recurrence intervals (Hodge et al., 2015).

There are few geodetic studies around the Malawi Rift. Sella et al., (2002) produced a global plate motion model using GPS, but it contained few sites on Nubia with the distribution heavily biased towards southern Nubia, only two sites to constrain the motion of Somalia, and no sites near Malawi. Fernandes et al., (2004) improved upon Sella et al., (2002) by increasing the number of GPS sites and increasing the timespan of data used at those sites. Calais et al., (2006) increased the number of sites from previous models and subdivided the region to include independent Victoria and Rovuma plates (Figure 1), but coverage around Malawi remained sparse. Stamps et al., (2008) combined an updated GPS dataset, DORIS, earthquake slip vectors, spreading rates, and transform fault azimuths in an inversion to solve for tectonic motions across the East African Rift, but there were still data gaps, particularly around the southern section of the Western Rift. Only a single campaign GPS site was used near Malawi, and only a combined total of 8 campaign and continuous GPS sites within the East African Rift. Despite these limitations, Stamps et al., (2008) further subdivided the region by adding the Lwandle plate (Figure 1). Saria et al., (2013) greatly improved on the number and time span of data from continuous GPS stations, utilized a network of campaign GPS sites, and increased the amount of DORIS data compared to previous works leading to more robust estimates of motion in the region. Data constrains around the Malawi remained sparse. Saria et al., (2014) improved on their 2013 work by incorporating more campaign GPS data, earthquake slip vector directions, transform fault azimuths, and spreading rates along the Southwest Indian Ridge into a block model following the methods of McCaffrey (2002). This led to improved Euler pole locations and angular velocities, but GPS data in the area surrounding Malawi Rift was still sparse with only a handful of short time span sites.

In this work, I utilize a new GPS dataset to improve upon previous geodetic works. I use more continuous GPS stations in the Malawi region as a result of the SEGMeNT project. In addition to the new stations, existing stations now have much longer time series than in previous studies, with 6+ more years of data at some sites, leading to decreased uncertainties and improved confidence in velocities across a slowly moving region. Also as a result of the SEGMeNT project, there is more seismic data in the region to help constrain fault locations and geometries used in my models. Together, these developments provide major improvements from previous studies.

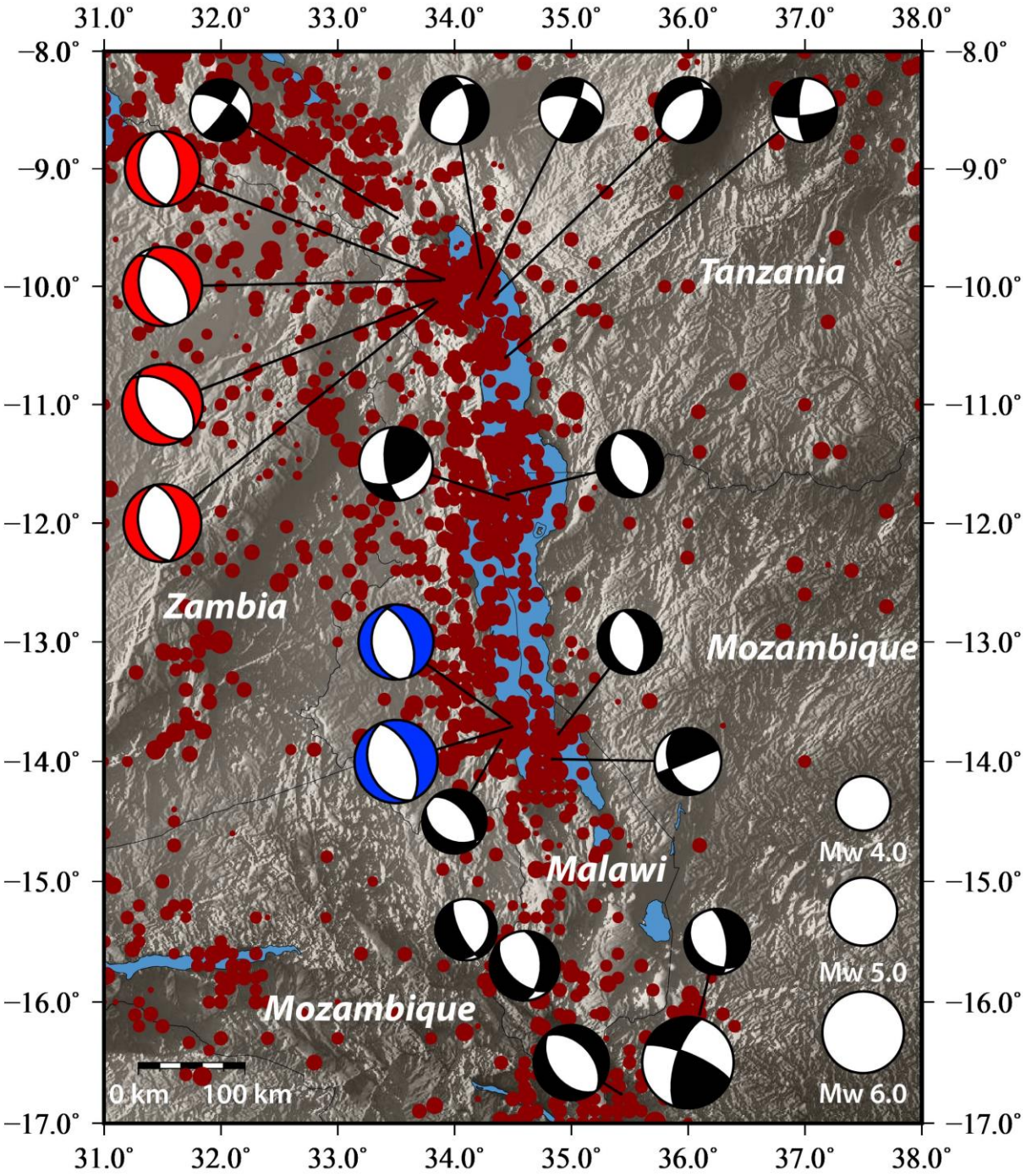

Figure 3 The area surrounding Lake Malawi showing seismicity in the area. Red focal mechanisms show the events in the 2009 Karonga Earthquakes. Blue focal mechanisms show the March 1989 Salima-Dedza-Mchinji Earthquakes. Black focal mechanisms are other selected events. RVP is Rungwe Volcanic Province. Data is selected from Craig et al. (2011), Delvaux and Barth (2010), USGS, U.S. Department of the Interior U.S. Geological Survey (2018), and Williams et al., (2019).

3. GPS DATA

Data from a total of 114 GPS stations was used in the model presented in this study (Table 1; Figures 4-7). The vast majority of the sites are located in Africa, but data from South America, Eurasia, and Antarctica was also used in order to constrain the motion of neighboring tectonic plates. Of the total, 12 sites were installed as part of the SEGMENT project (Figure 1). Other data came from a variety of networks including Africa Array, the Global GNSS Network (GGN), and the International GNSS Service (IGS). All data used is publicly accessible through UNAVCO. The time span of data available varies for each site, but the dataset has an overall stop date of March 2019. All sites have at least a two-year data span with some sites having more than 19 years of data. The average site data time span is 10.5 years. Some of the data has been previously published (e.g. Stamps et al., 2008; Stamps et al., 2018; Saria et al., 2013; Saria et al., 2014), but the dataset presented here includes additional data (new sites as well as additional data from existing sites) and has been reprocessed. Table A.1 lists the references and doi's for the sites used in this study.

The GPS data was analyzed using the GIPSY/OASIS goa-5.0 software in point positioning mode and the standard solution strategy discussed in Fu and Freymueller (2012) and Fu et al. (2012). In this strategy, each day of data from a site is processed independently before all sites for a given data are merged into a combined solution that is aligned with the ITRF2008 reference frame. This frame alignment is computed each day through a large number of sites used in the ITRF realization. The daily solutions were then combined in a least squares inversion to estimate linear, long-term velocities at each site. The velocities were then transformed into a Nubia-fixed reference frame. Initially, the Nubia estimate from the GEODVEL plate motion model (Argus et al. 2010) was used, but this model produced small, coherent patterns of motion in regions that should have been stable, such as South Africa and western Africa. The GEODVEL model did not use many sites from Nubia and most were in South Africa, potentially creating a bias in the reference frame. To overcome this issue, a new estimate of Nubia motion was performed. Sites used in the estimate were chosen based on time series length, linearity of time series, and location to ensure a distribution of sites across stable Nubia. Velocities and uncertainties in the ITRF frame from these sites were then used in a simple least squares inversion to estimate an Euler pole for Nubia. This pole was then used to reference velocities from the full datasets to stable Nubia.

Table 1 GPS Sites used in this study

Site Name	Longitude (˚E)	Latitude (˚N)	East Velocity (mm/yr)	North Velocity (mm/yr)	East σ	North σ	East-North Velocity Correlation
ABOO	37.80943	8.99211	-0.34872	0.72937	0.46	0.42	0.12966
ABPO	47.22921	-19.01831	1.46462	0.41986	0.44	0.49	0.12661
ADIS	38.76630	9.03514	1.43434	2.63201	0.46	0.42	0.12554
ARTU	58.56045	56.42982	0.98266	-6.06006	0.43	0.43	-0.01211
ASC1	-14.41207	-7.95122	-29.08050	-6.12411	0.53	0.43	0.32030
ASCG	-14.33266	-7.91628	-27.63450	-5.37459	0.55	0.43	0.29964
ASOS	34.55294	10.05059	-0.30807	0.82509	0.47	0.42	0.13945
BAHR	50.60812	26.20914	5.70437	15.49270	0.46	0.41	0.03073
BDAR	37.35966	11.59982	-2.33199	1.09011	0.47	0.42	0.12054
BDMT	37.35966	11.59982	-1.06199	2.02011	0.47	0.42	0.12175
BJAB	2.00053	7.18235	0.99607	0.45066	0.49	0.40	0.29053
BJCO	2.45002	6.38466	0.08050	-0.10767	0.49	0.40	0.29203
BJFS	115.89248	39.60860	-2.43000	-4.58000	1.00	1.00	0.00000
BJKA	2.92798	11.12474	-0.13729	-0.23412	0.49	0.39	0.27521
BJNA	1.38075	10.25318	0.21821	0.54854	0.49	0.40	0.28290
BJNI	3.20404	9.95128	0.08213	-0.08439	0.49	0.40	0.27745
BJPA	2.62566	9.35751	0.61373	-0.01356	0.49	0.40	0.28218
BJSA	1.99320	7.92777	0.29505	-0.16882	0.49	0.40	0.28812
BRAZ	-47.87796	-15.94737	-29.88800	2.08108	0.54	0.44	0.22952
CAS1	110.51919	-66.28289	9.33784	-5.49427	0.44	0.46	-0.32087
CGGN	9.11831	10.12309	2.38067	0.32031	0.51	0.40	0.24242
CTPM	33.26300	-9.70140	-1.08356	-0.56185	0.47	0.46	0.20105
DAKA	-17.46483	14.68496	-0.25221	0.86591	0.56	0.41	0.27500
DAKR	-17.43947	14.72124	0.13465	0.27218	0.51	0.40	0.31141
DAV1	77.97415	-68.57788	4.90621	-11.92270	0.39	0.52	-0.14739
DEAR	23.99264	-30.66521	-0.34754	0.50292	0.46	0.48	0.28848
DJIG	42.84707	11.52629	6.98590	2.23454	0.47	0.42	0.09674

Site Name	Longitude (˚E)	Latitude (˚N)	East Velocity (mm/yr)	North Velocity (mm/yr)	East σ	North σ	East-North Velocity Correlation
DODM	35.74817	-6.18646	2.03428	0.96558	0.46	0.45	0.18267
ETAD	38.76282	9.01986	0.45599	1.32144	0.46	0.42	0.12422
ETDD	41.85835	9.61307	4.32450	-0.90356	0.47	0.43	0.10386
ETJI	36.81741	7.66786	0.72938	0.80563	0.56	0.44	0.11043
FLRS	-31.12639	39.45384	-19.11080	5.87964	0.53	0.41	0.27355
FUNC	-16.90762	32.64795	-0.84183	0.92714	0.51	0.38	0.25633
GINR	40.70842	7.14600	4.91381	1.73532	0.48	0.43	0.11160
GMAS	-15.63427	27.76479	1.14649	0.62255	0.50	0.38	0.27758
GOUG	-9.88072	-40.34883	0.44529	0.25585	0.51	0.45	0.30911
HARB	27.70724	-25.88696	0.22863	0.52699	0.45	0.48	0.26669
HNUS	19.22306	-34.42463	-0.31640	0.44182	0.46	0.48	0.30947
HRAO	27.68714	-25.88962	2.02660	0.10491	0.45	0.48	0.26680
IFRN	-5.10846	33.53962	0.63994	-0.84298	0.49	0.37	0.20270
ISOK	32.64559	-10.17108	0.85681	0.43675	0.50	0.47	0.18701
KARO	33.89550	-9.95410	1.68885	-1.63615	0.46	0.46	0.19937
KERG	70.25552	-49.35147	3.81582	-11.89070	0.40	0.53	-0.07064
KFNY	35.10255	-9.54680	2.86653	0.39290	0.46	0.46	0.19245
KOUR	-52.80596	5.25218	-25.15750	4.12623	0.53	0.46	0.27955
KUNM	102.79719	25.02954	-0.77000	-5.57000	1.00	1.00	0.00000
LIVA	34.10710	-10.61370	-0.04543	0.18319	0.47	0.46	0.19579
LPAL	-17.89384	28.76396	0.56152	0.56922	0.50	0.39	0.28265
MAD2	-4.24966	40.42916	4.22711	-1.93391	0.48	0.36	0.15808
MAL2	40.19414	-2.99606	3.38841	0.90707	0.46	0.45	0.14921
MALI	40.19520	-2.99539	5.05830	0.38725	0.46	0.45	0.14760
MAS1	-15.63328	27.76374	0.37603	0.41241	0.50	0.38	0.27814
MATE	16.70446	40.64913	4.31174	0.62331	0.46	0.37	0.04685
MATL	34.58467	-9.59204	1.77037	0.26940	0.46	0.46	0.19708
MAW1	62.87072	-67.60477	1.88007	-13.19840	0.38	0.53	0.00004
MAYG	45.25815	-12.78205	1.96024	-1.35973	0.47	0.48	0.12745

Site Name	Longitude (˚E)	Latitude (˚N)	East Velocity (mm/yr)	North Velocity (mm/yr)	East σ	North σ	East-North Velocity Correlation
MBAR	30.73788	-0.60147	2.37837	0.28567	0.46	0.43	0.19872
MBBC	34.80028	-11.27364	-0.73770	-0.10957	0.46	0.46	0.19868
MFKG	25.53997	-25.80502	-0.17723	1.21448	0.46	0.48	0.27585
MONG	23.15074	-15.25412	1.13197	1.67288	0.47	0.46	0.26790
MPIK	31.45121	-11.82098	0.21549	1.47532	0.55	0.48	0.18461
MTDK	36.42056	-7.54399	3.15943	-0.62436	0.46	0.45	0.18096
MZUZ	34.00595	-11.42510	1.60827	0.87955	0.46	0.46	0.20347
NAMA	42.04465	19.21142	10.34120	11.90380	0.46	0.41	0.07736
NAZR	39.29057	8.56774	3.31869	0.55745	0.46	0.42	0.12423
NEGE	39.58941	5.33465	4.52325	0.72610	0.46	0.43	0.13112
NIAM	2.18319	13.47926	0.12717	0.52558	0.50	0.39	0.26461
NKLG	9.67213	0.35391	-0.04516	0.49876	0.48	0.41	0.28874
NOT1	14.98979	36.87584	2.18897	1.00476	0.47	0.37	0.08153
NURK	30.08968	-1.94455	3.05379	0.22883	0.47	0.43	0.20424
OHI2	-57.90133	-63.32108	-10.18980	2.82896	0.50	0.41	-0.05184
OHI3	-57.89929	-63.32035	-10.37970	1.94835	0.50	0.41	-0.05180
OHIG	-57.90027	-63.32070	-9.95978	2.97864	0.67	0.55	-0.01549
ONSA	11.92551	57.39530	4.30522	-4.00669	0.46	0.37	-0.05824
PDEL	-25.66277	37.74775	1.35483	0.95222	0.50	0.39	0.28378
POTS	13.06609	52.37930	4.43849	-3.26081	0.46	0.37	-0.02586
PRE1	28.22404	-25.74635	0.70118	0.70132	0.45	0.48	0.26344
RABT	-6.85429	33.99810	0.52829	-0.26169	0.49	0.37	0.21125
RAMO	34.76314	30.59761	1.23688	2.80775	0.45	0.39	0.05297
RBAY	32.07838	-28.79555	0.40052	0.47528	0.45	0.49	0.24554
RCMN	36.89348	-1.22083	4.53518	0.46625	0.46	0.44	0.16475
REUN	55.57172	-21.20823	0.80213	-0.66093	0.44	0.50	0.06267
ROBE	40.02611	7.11340	5.77139	-1.82057	0.46	0.43	0.12430
SBOK	17.87921	-29.66932	-0.29265	0.52596	0.47	0.47	0.31033
SERB	37.02200	12.51160	-0.08401	1.06848	0.53	0.43	0.11207

Site Name	Longitude (˚E)	Latitude (˚N)	East Velocity (mm/yr)	North Velocity (mm/yr)	East σ	North σ	East-North Velocity Correlation
SEY1	55.47930	-4.67360	3.77015	-1.47830	0.46	0.47	0.05264
SHAO	121.20044	31.09964	-1.97000	-4.11000	1.00	1.00	0.00000
SHIS	38.98811	11.98505	-0.80610	1.02906	0.48	0.42	0.11604
SIMO	18.43957	-34.18794	0.00854	0.72882	0.46	0.48	0.31268
SNGC	35.67276	-10.68980	-1.25415	1.30583	0.46	0.46	0.19275
SOLA	46.40057	24.91068	6.99793	14.53740	0.46	0.41	0.04473
STHL	-5.66735	-15.94253	0.42702	0.18946	0.51	0.44	0.33122
SUTH	20.81046	-32.38021	0.36114	0.71703	0.46	0.48	0.30413
SVTL	29.78074	60.53285	3.90636	-6.31226	0.44	0.41	-0.10790
SYOG	39.58374	-69.00696	-2.89169	-13.24780	0.40	0.51	0.20909
TAMA	-0.86172	9.55426	-0.32932	-0.13626	0.50	0.40	0.28662
TANZ	39.20793	-6.76559	2.27080	0.39341	0.46	0.46	0.16182
TDOU	30.38401	-23.07991	0.89394	-0.62756	0.45	0.48	0.24662
TEZI	26.01573	-15.74653	0.50537	0.89191	0.47	0.46	0.25709
TGCV	-22.98276	16.75477	1.63113	0.09970	0.52	0.41	0.31792
TNDC	37.34053	-11.06260	1.97936	0.10694	0.46	0.46	0.18274
UKAM	25.00307	-8.73264	2.09409	1.90572	0.65	0.49	0.16773
ULUB	27.48494	-11.63056	4.31232	0.47503	0.48	0.46	0.23053
VACS	57.49704	-20.29708	0.94251	-1.54684	0.44	0.50	0.04647
VOIM	46.79327	-21.90630	0.94982	-0.77621	0.45	0.50	0.12998
VWZM	33.57440	-11.17530	-3.15912	-0.06944	0.46	0.46	0.20444
WIND	17.08943	-22.57492	0.08140	1.11277	0.47	0.46	0.30740
WSRT	6.60450	52.91461	4.74428	-2.27121	0.47	0.37	0.00086
WUHN	114.35726	30.53165	-1.65000	-4.71000	1.00	1.00	0.00000
XIAN	109.22150	34.36867	-1.71000	-5.12000	1.00	1.00	0.00000
YIBL	56.11233	22.18646	7.91756	19.09860	0.46	0.42	0.02364
YKRO	-5.24009	6.87056	0.42612	0.07003	0.50	0.40	0.30824
ZAMB	28.31101	-15.42554	0.12250	0.62359	0.46	0.46	0.24699
ZOMB	35.32513	-15.37584	1.05309	0.26734	0.45	0.47	0.20419

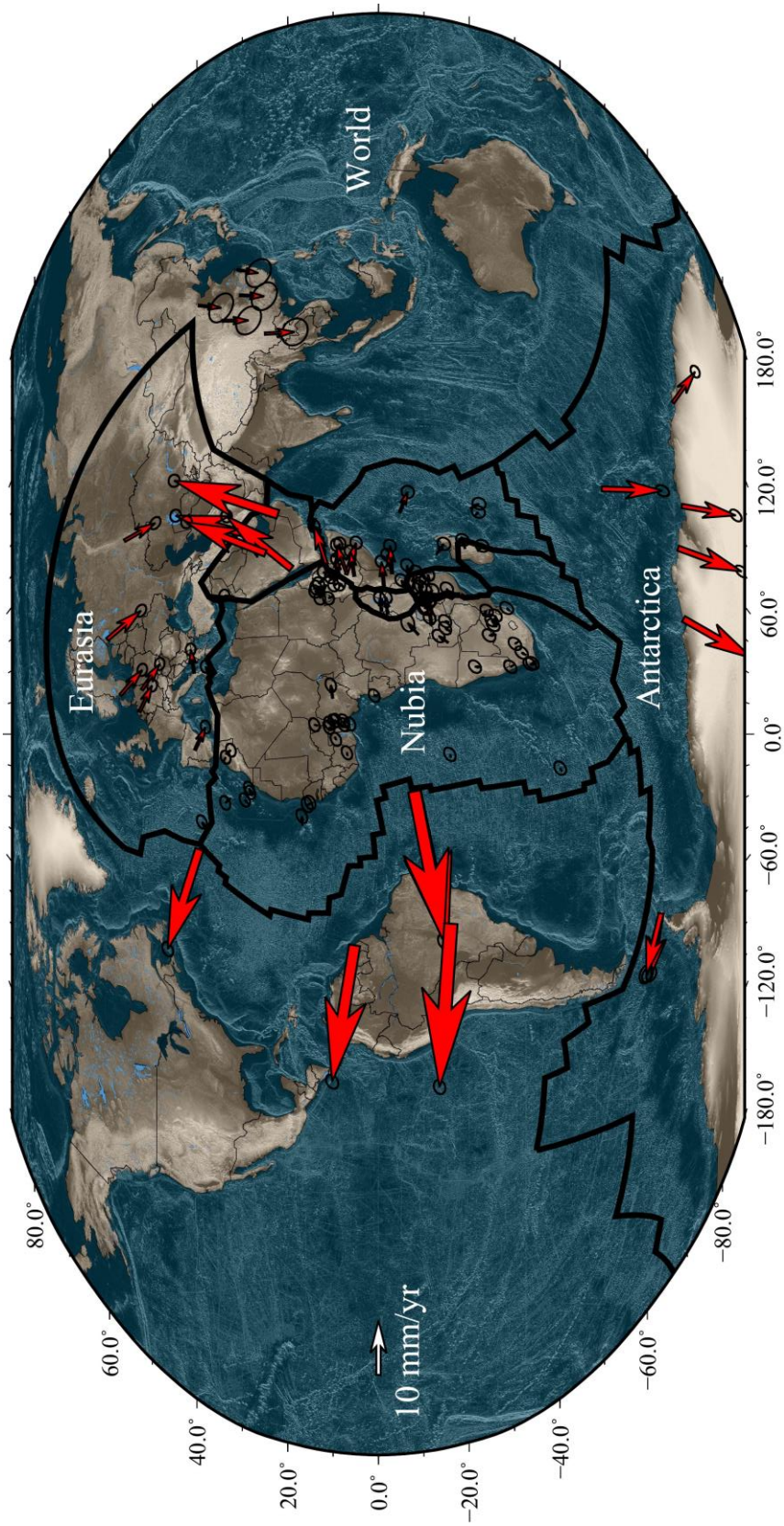

Figure 4 Global GPS velocities used in this study. Black lines indicate block boundaries used in this model. Velocities are relative to Nubia.

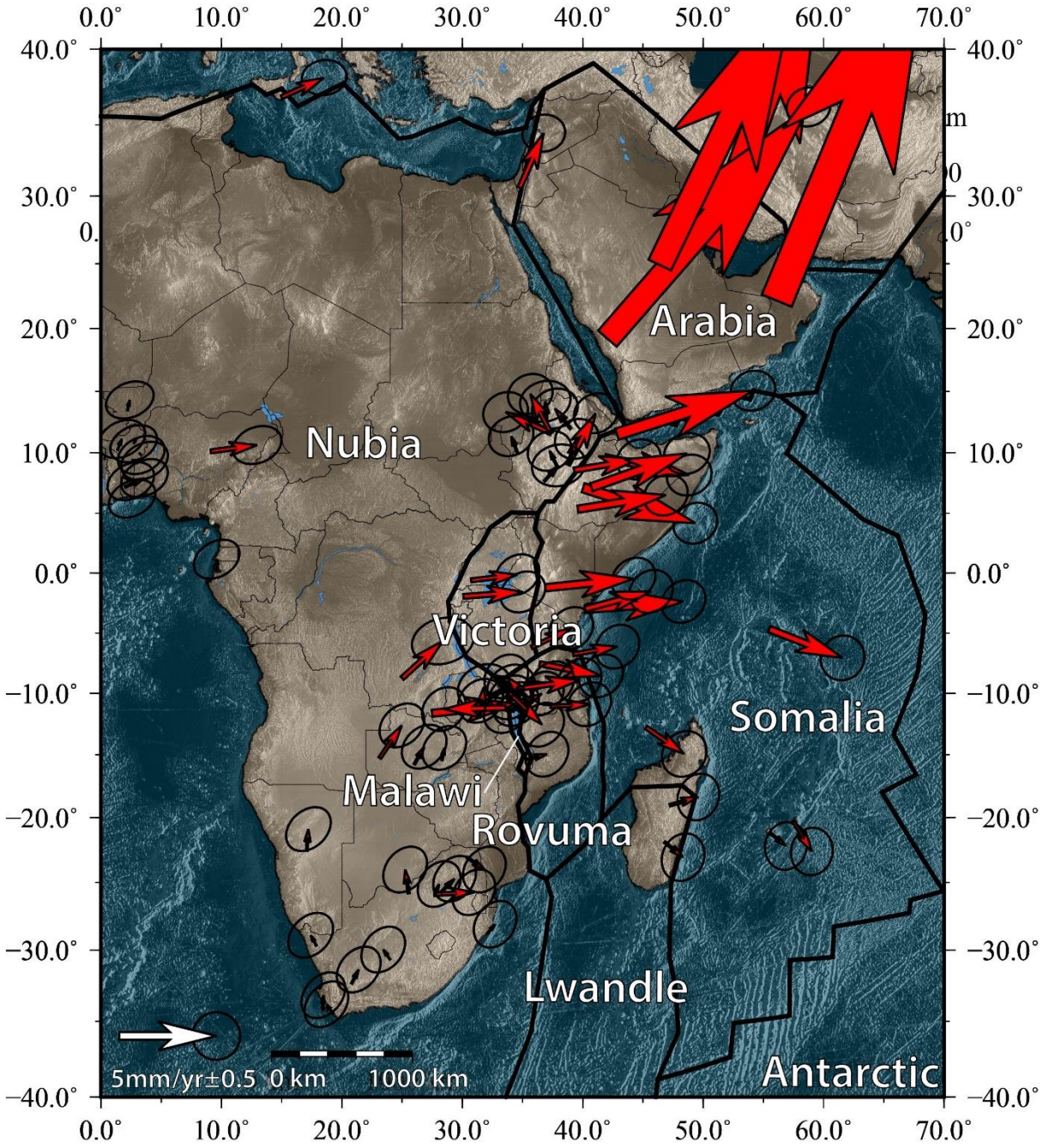

Figure 5 GPS velocities on Nubia and other plates near the East African Rift. Black lines indicate block boundaries used in this model. Velocities are relative to Nubia.

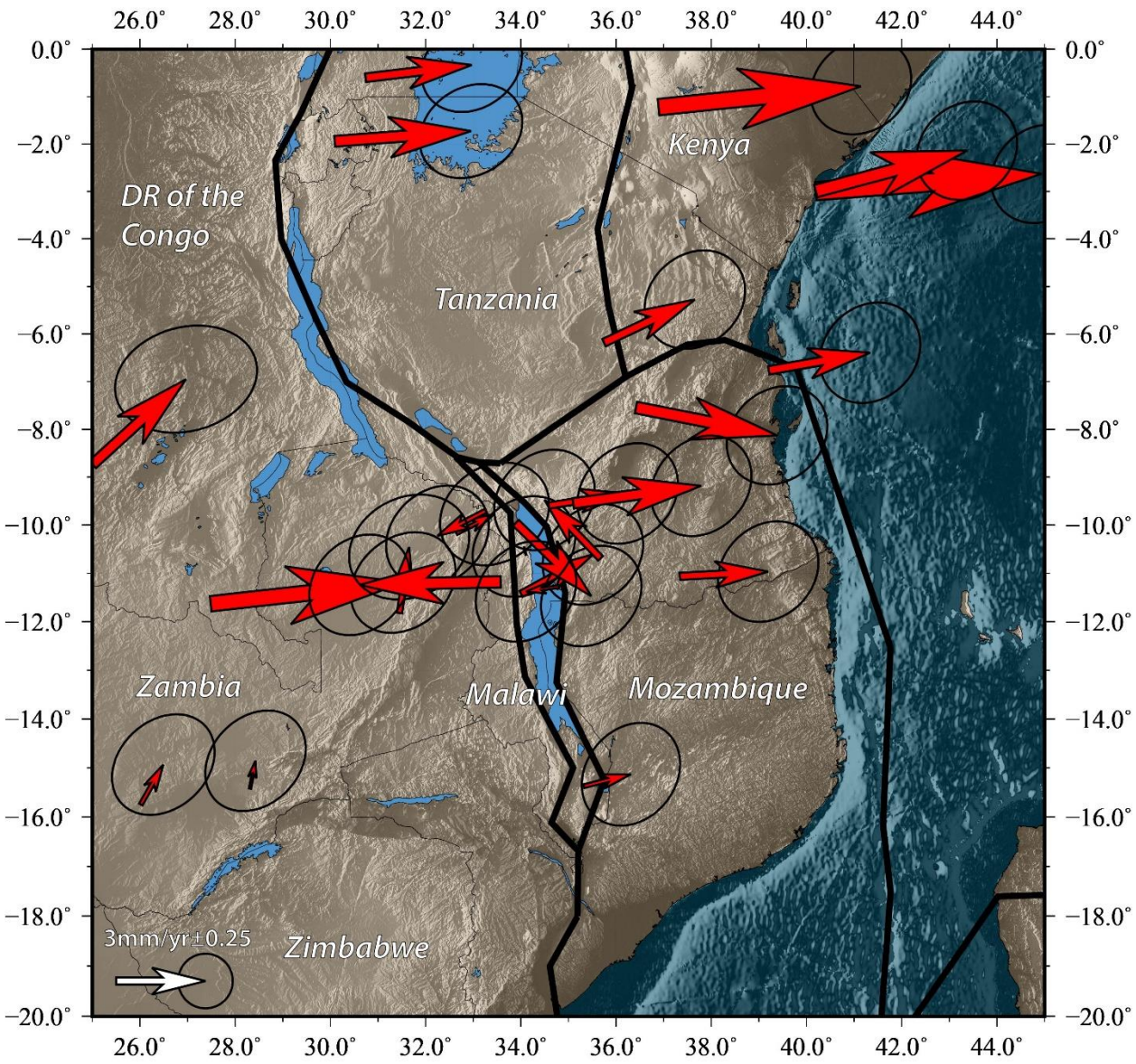

Figure 6 GPS data surrounding the Malawi Rift. Black lines indicate block boundaries used in this model. Velocities are relative to Nubia.

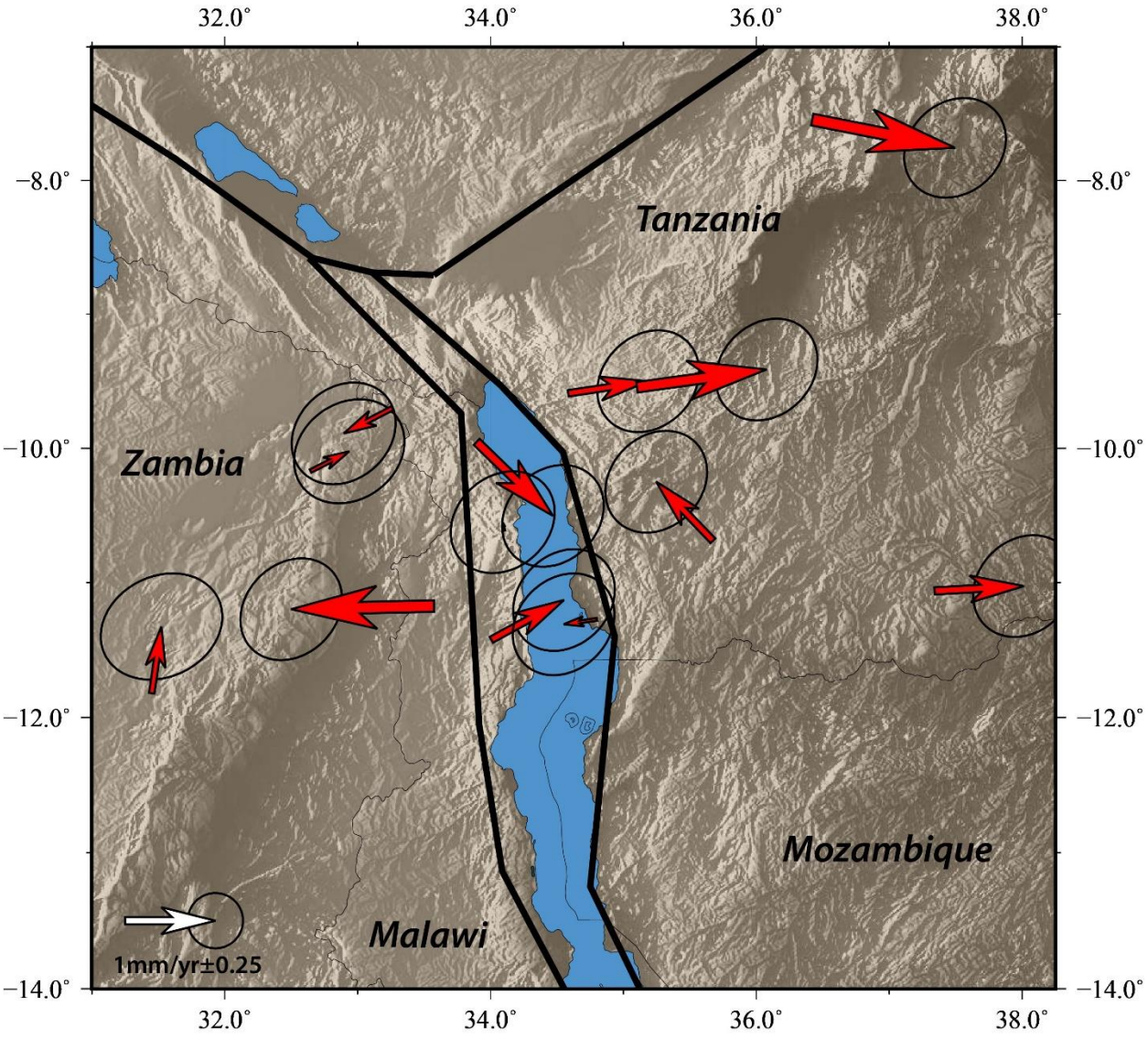

Figure 7 GPS velocities around Northern Malawi. Black lines indicate block boundaries used in this model. Velocities are relative to Nubia.

4. METHODS

Geodynamic modeling of plate boundaries can be separated into different groups based on the approach used to model the observed surface motion. Continuum modeling (e.g. Flesch et al., 2000; Holt et al., 2000) utilizes the idea that surface motions of the earth are based on a viscous mantle flowing beneath a thin sheet. Block models (e.g. Loveless & Meade, 2010; Meade & Hager, 2005) assume that the earth is broken up into small plates that behave fairly rigidly. Surface deformation in block models results from a combination of rigid block rotation and elastic deformation along the block boundaries.

To determine where to put block boundaries, both interseismic velocities and geologic information must be considered. In most cases, similar velocities can be grouped onto the same block as block modeling assumes that the interiors of blocks are mostly rigid and moving together. In Figure 8 I demonstrate this by presenting an interseismic velocity field and grouping the velocities based on similar orientation and magnitude. For example, the red vectors in the top left corner are grouped based on their similar northeast velocities. These vectors are significantly different from the blue vectors below, potentially suggesting there is a boundary between the two. While the GPS data may suggest a boundary, it is imperative to incorporate other datasets into the model to constrain the boundaries. Geological or additional geophysical data could provide insight into fault systems, topography, or earthquakes that could suggest a specific configuration of boundaries. These boundaries may generalize fault systems; individual faults are often too small to be explicitly defined outside the area of interest.

I apply the block modeling techniques of Meade & Loveless, (2009) to the Malawi Rift. This technique uses GPS velocity fields and fault geometries to simultaneously solve for fault slip rates and block motions, allowing for a kinematically consistent estimate of motion across the region. A brief summary of Meade & Loveless, (2009) is below.

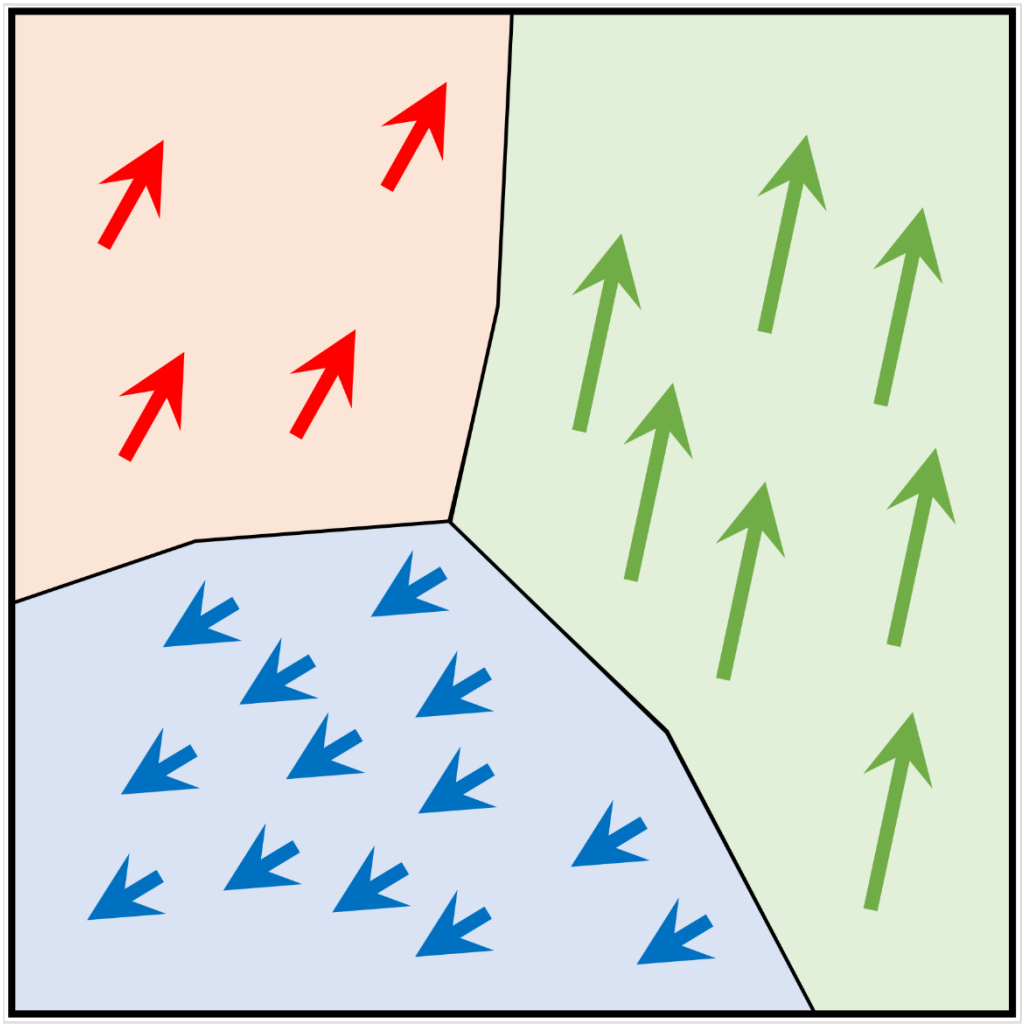

Figure 8 A simplified example of a block model. Each block is divided based on the direction and magnitude of similar velocities and geologic information.

4.1 Block Modeling Summary

Block modeling utilizes GPS data to determine block rotation ($\tilde{\boldsymbol{v}}_{\boldsymbol{B}}$) and elastic deformation ($\tilde{\boldsymbol{v}}_{\boldsymbol{CSD}}$) in the estimation of the interseismic velocity ($\tilde{\boldsymbol{v}}_{\boldsymbol{I}}$), modified from Meade and Loveless, (2009).

$$\tilde{\boldsymbol{v}}_{\boldsymbol{I}} = \tilde{\boldsymbol{v}}_{\boldsymbol{B}} - \tilde{\boldsymbol{v}}_{\boldsymbol{CSD}} \tag{1}$$

Expressing the block rotation as linear operators yields:

$$\tilde{\boldsymbol{v}}_{\boldsymbol{B}} = \boldsymbol{P}_{\boldsymbol{V}}\boldsymbol{G}_{\boldsymbol{B}}\boldsymbol{\Omega} = \begin{bmatrix} -\sin\phi\cos\theta & -\sin\phi\sin\theta & \cos\phi \\ -\sin\theta & \cos\theta & 0 \\ -\cos\phi\cos\theta & -\cos\phi\sin\theta & -\sin\phi \end{bmatrix} \begin{bmatrix} 0 & \hat{z} & -\hat{y} \\ -\hat{z} & 0 & \hat{x} \\ \hat{y} & -\hat{x} & 0 \end{bmatrix} \begin{bmatrix} \Omega_{\hat{x}} \\ \Omega_{\hat{y}} \\ \Omega_{\hat{z}} \end{bmatrix} \tag{2}$$

where $\mathbf{P_V}$ is the conversion from cartesian to east north up, $\boldsymbol{G}_{\boldsymbol{B}}$ is the cross product, and $\boldsymbol{\Omega}$ is the angular velocity.

The elastic deformation term in (1), $\tilde{\boldsymbol{v}}_{\boldsymbol{CSD}}$, represents the effects of strain accumulation on locked faults in the interseismic period of the earthquake cycle. This term can be written as:

$$\tilde{\boldsymbol{v}}_{\boldsymbol{CSD}} = \boldsymbol{P}_{\boldsymbol{\alpha}}\boldsymbol{G}_{\boldsymbol{O}}\mathbf{s} = \begin{bmatrix} \cos\alpha & -\sin\alpha & 0 \\ \sin\alpha & \cos\alpha & 0 \\ 0 & 0 & 1 \end{bmatrix} \begin{bmatrix} \partial\bar{V}_{\bar{x}}/\partial\bar{S}_{\bar{s}} & \partial\bar{V}_{\bar{x}}/\partial\bar{S}_{\bar{d}} & \partial\bar{V}_{\bar{x}}/\partial\bar{S}_{\bar{t}} \\ \partial\bar{V}_{\bar{y}}/\partial\bar{S}_{\bar{s}} & \partial\bar{V}_{\bar{y}}/\partial\bar{S}_{\bar{d}} & \partial\bar{V}_{\bar{y}}/\partial\bar{S}_{\bar{t}} \\ \partial\bar{V}_{\bar{z}}/\partial\bar{S}_{\bar{s}} & \partial\bar{V}_{\bar{z}}/\partial\bar{S}_{\bar{d}} & \partial\bar{V}_{\bar{z}}/\partial\bar{S}_{\bar{t}} \end{bmatrix} \begin{bmatrix} S_s \\ S_d \\ S_t \end{bmatrix} = \boldsymbol{G}_{\boldsymbol{\alpha O}}\mathbf{s}, \tag{3}$$

where $\boldsymbol{P}_{\boldsymbol{\alpha}}$ is a rotation matrix that transforms from Cartesian space to geographic coordinates, $\boldsymbol{G}_{\boldsymbol{O}}$ is the elastic Green's functions describing a stations response to slip on a fault (Okada, 1985), **s** is slip, $\boldsymbol{G}_{\boldsymbol{\alpha O}}$ is the Green's function in terms of the rotation matrix, and $\boldsymbol{S}_{\boldsymbol{s}}, \boldsymbol{S}_{\boldsymbol{d}}, \boldsymbol{S}_{\boldsymbol{t}}$ are the respective strike slip, dip slip, and tensile slip components of slip.

Substituting the equations 2 and 3 into equation 1 yields:

$$\tilde{\boldsymbol{v}}_{\boldsymbol{I}} = \tilde{\boldsymbol{v}}_{\boldsymbol{B}} - \tilde{\boldsymbol{v}}_{\boldsymbol{CSD}} = \left[\boldsymbol{P}_{\boldsymbol{V}}\boldsymbol{G}_{\boldsymbol{B}} - \boldsymbol{G}_{\boldsymbol{\alpha O}}\boldsymbol{P}_{\boldsymbol{F}}\boldsymbol{P}_{\boldsymbol{V_2}}\boldsymbol{P}_{\boldsymbol{\Delta\hat{v}}}\right][\boldsymbol{\Omega}]. \tag{4}$$

Where $\boldsymbol{P}_{\boldsymbol{F}}$ is the conversion from east north to strike and dip, $\boldsymbol{P}_{\boldsymbol{V_2}}$ is the conversion from Cartesian space to east north, and $\boldsymbol{P}_{\boldsymbol{\Delta\hat{v}}}$ is the projection of differential block motion to fault slip. $\tilde{\boldsymbol{v}}_{\boldsymbol{I}}$ is the observed data vector; a combination of velocities ($\tilde{\boldsymbol{v}}_{\boldsymbol{GPS}}$) and fault slip constraints ($\boldsymbol{s}_{\boldsymbol{obs}}$). The general equation solving for angular velocities ($\boldsymbol{\Omega}^{\boldsymbol{est}}$) is:

$$[\boldsymbol{\Omega}^{\boldsymbol{est}}] = (\boldsymbol{G}^{\boldsymbol{T}}\boldsymbol{W}\boldsymbol{G})^{-1}\boldsymbol{G}^{\boldsymbol{T}}\boldsymbol{W}\begin{bmatrix} \tilde{\boldsymbol{v}}_{\boldsymbol{GPS}} \\ \boldsymbol{s}_{\boldsymbol{obs}} \\ 0 \end{bmatrix}. \tag{5}$$

With $\boldsymbol{W}$ as the inverse of the data covariance matrix ($\boldsymbol{C}_{\boldsymbol{GPS}}$) and the covariance for *a priori* slip constraints ($\boldsymbol{C}_{\boldsymbol{obs}}$), seen in equation 6.

$$\boldsymbol{W} = \begin{bmatrix} \boldsymbol{C_{GPS}}^{-1} & 0 \\ 0 & \boldsymbol{C_{obs}}^{-1} \end{bmatrix} \quad (6)$$

I am not using the vertical component of the data vectors because there are complex seasonal signals, primarily in the vertical component, that were difficult to model. Meade & Loveless, (2009) also allows for the calculations of intrablock strain however I did not utilize this due to the data density.

4.2 Fault Geometries and Block Boundaries

I incorporate multiple types of data including geologic maps, geophysical models, and topography to constrain fault locations, dips, and locking depths. I then use an iterative process to determine the best fit with the GPS data. These block and fault geometries can be grouped into three main groups: far field, near field, and as a subset of the near field but the focus of this study, Malawi.

4.2.1 Far Field Blocks

The locations of the far field faults (Figure 9) are guided by the boundaries in Bird, (2003). Generalizations have been made to many of these faults where similar structures have been combined. As locking depths and dip angles are poorly constrained in the East African Rift, I follow similar iterative methods to Saria et al., (2014) and assign a dip of 70° and a locking depth of 15 km for far field faults. Exceptions to these methods are listed in the individual sections.

Arabia, Eurasia, and Antarctica are all considered to be far field blocks for this model. The Arabian boundary with Nubia starts at the Afar triple junction where it follows the Red Sea Northwest before turning north to connect with the Zagros Mountains. The border between the Arabian and Eurasian blocks connects the Gulf of Oman, Arabian Sea, and Gulf of Aden before reconnecting at the Afar Triple Junction. The boundary of the Eurasian block starts in Anatolia and follows the Mediterranean Sea west until it connects with the Mid-Atlantic Ridge. It then follows the ridge north past Iceland before connecting with eastern Asia and then terminating in the Arabian Sea. The Antarctic block boundary follows the Antarctic Ridge.

4.2.2 Near Field Blocks

Near field blocks include the Somalia, Victoria, Rovuma, Lwandle, and Nubia blocks (Figure 9). Due to the proximity of these blocks to Malawi and the amount of information available, geometries of these blocks are discussed in detail. Where available data on fault segments is sparse, dips and locking depths were the same as used in far field blocks

The Somalian Plate has eastern and southern boundaries with the Austro-Indian and Antarctic plates, respectively, following mid ocean ridges similar to Bird (2003). The northern boundary in the Gulf of Aden is based on a modified version of Bird (2003) that more closely follows the spreading centers. The Somalian plate borders the Nubian plate in Ethiopia where the boundary follows the Main Ethiopian Rift until the Victoria plate (Figure 9). The western boundary will be discussed below.

The boundaries of the Victoria block diverge from the Bird (2003) model significantly by including boundaries on the Eastern Rift and between the Victoria and Rovuma microplates (Figure 9, Figure 10). In northern Victoria, Stamps et al., (2008) followed Bird (2003) in creating a boundary that followed seismicity in the north, but both interpolated across a large, poorly constrained aseismic zone. Saria et al., (2013; 2014) follow a different interpretation across the aseismic zone that does not connect to the seismicity in South Sudan. I follow a modified version of Saria et al., (2014) that smooths the boundary in this area because it is still poorly constrained. In the present model, the southwestern boundary of the Victoria block follows the seismicity (Figure 10) (Craig et al., 2011; Delvaux & Barth, 2010) and rift lakes until southern Lake Tanganyika. There, the boundary follows the Chisi Suture Zone and the Ufipa border fault as a part of the Rukwa Rift (Heilman et al., 2019; Lavayssière et al., 2019). The eastern boundary follows volcanism, seismicity, and topography, based on (Saria et al., 2014).

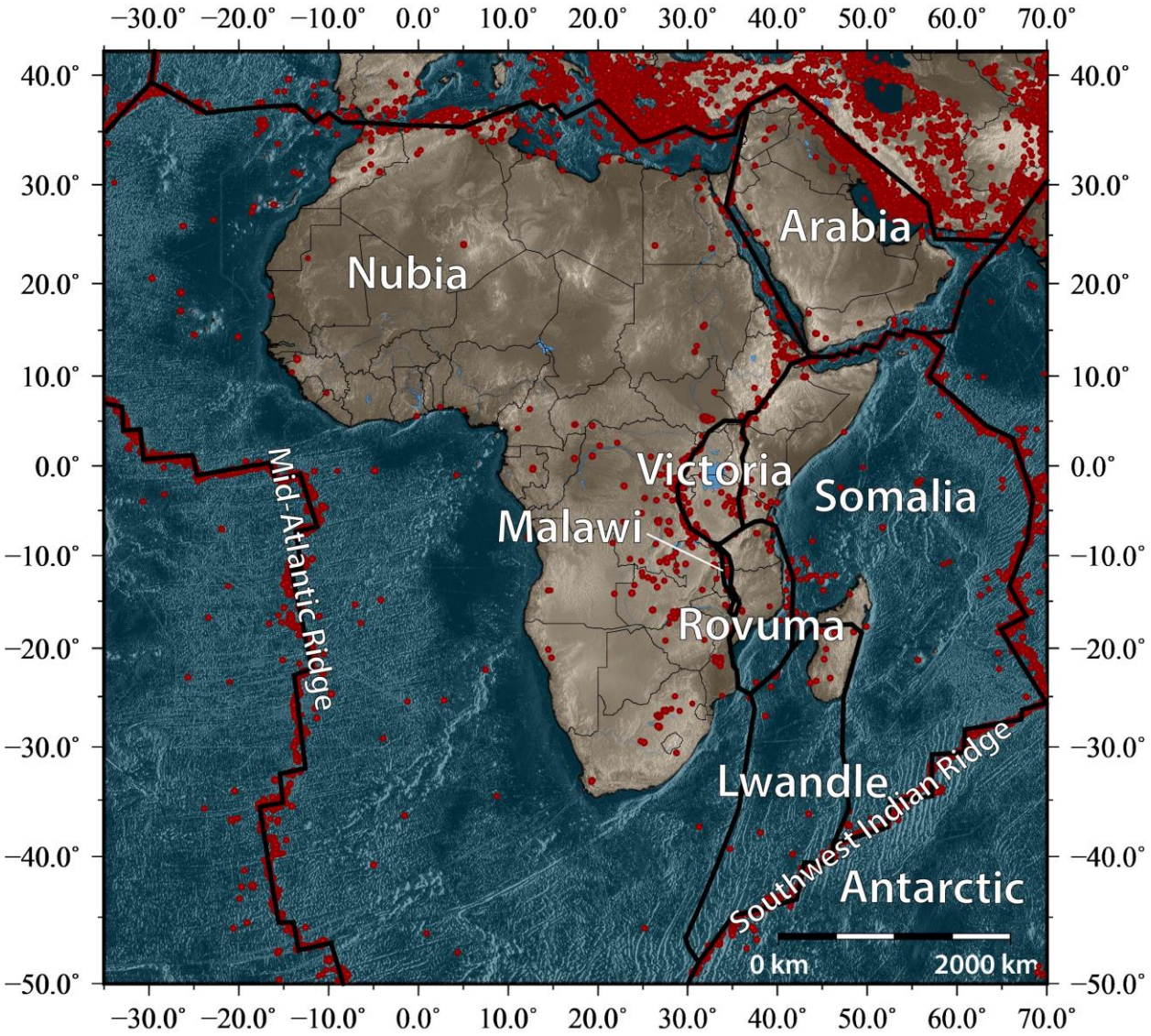

Figure 9 Major blocks used in this study. Black lines represent block boundaries, red circles represent selected background seismicity from the ISC-EHB catalog (Engdahl et al., 2020; International Seismological Centre, 2020; Engdahl et al., 1998; Weston et al., 2018).

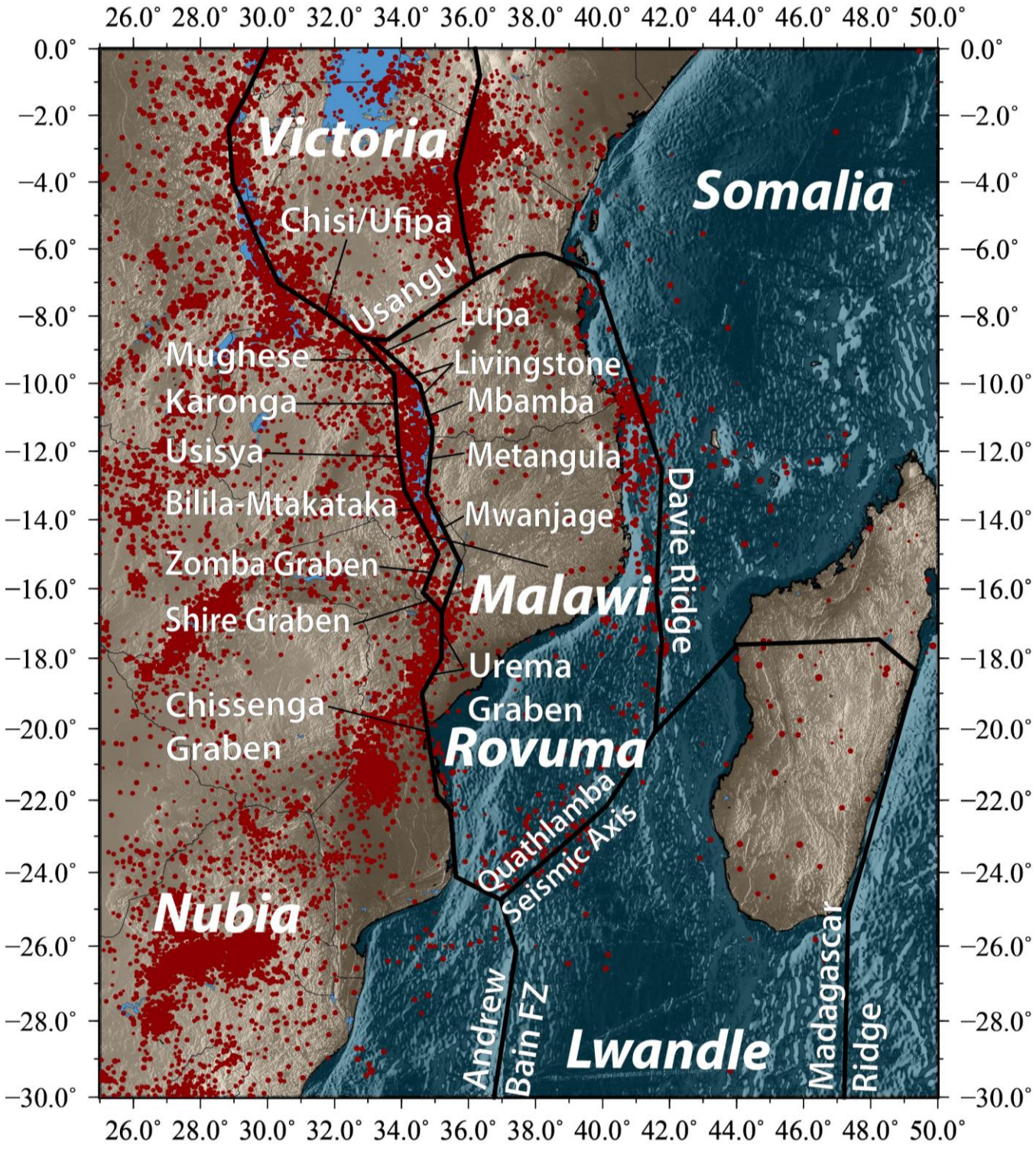

Figure 10 Major blocks and block boundaries for near field blocks. Major fault systems near Malawi are labeled.

I infer that the boundary between the Rovuma and Victoria blocks is the topographic low connecting the Usangu flats to the Ruaha Basin via the Proterozoic Usagaran Belt (Delvaux et al., 1992; Ebinger, 1989b; Le Gall et al., 2004; Saria et al., 2014; Stamps et al., 2008). Seismically, this boundary is difficult to interpret. Mulibo & Nyblade, (2016) use seismicity to suggest that the boundary is further south than used in Saria et al., (2014). I chose to follow the area between the two suggested boundaries in order to produce a model follows the topography and seismicity of the region (Figure 10). The Eastern boundary primarily follows the Davie Ridge (Chorowicz, 2005; Franke et al., 2015) until it intersects a line of seismicity at the Quathlamba Seismic Axis (Déprez et al., 2013; Saria et al., 2014) where it connects to the Chissenga Graben. The boundary of the Rovuma plate south of Lake Malawi follows the Urema and Chissenga Grabens before connecting with the Quathlamba Seismic axis (Domingues et al., 2016; Lloyd et al., 2019; Williams et al., 2019).

Previous geologic studies defined the Lwandle plate through spreading ridges and transform fault azimuths (Horner-Johnson et al., 2005, 2007), as do previous geodetic studies (Saria et al., 2013, 2014; Stamps et al., 2008). The model southwestern boundary follows the Andrew Bain Fracture Zone based on Horner-Johnson et al., (2007) and Saria et al., (2014) connecting the Southwest Indian Ridge (SWIR) border to the Quathlamba Seismic Axis. The eastern boundary follows the Madagascar Ridge (Saria et al., 2013, 2014; Stamps et al., 2008).

4.2.3 The Malawi Block

The preferred model geometry required additional boundaries between the Rovuma and Nubia blocks based on the interseismic velocity field. Each boundary is discussed in detail below. I group the boundaries by three basins: the North Basin, Central Basin, and South Basin (Figure 1).

Prior to reaching Lake Malawi, the preferred northeastern model boundary starts at the southern end of the Rukwa Rift on the Lupa fault, which, based on the magnetic anomaly, is interpreted to connect to the Livingstone border fault in the North Basin across the Rungwe Volcanic Province (Heilman et al., 2019; Lavayssière et al., 2019; Lemna et al., 2019). The Livingstone Border Fault continues to propagate to the end of the North Basin. I set the locking depth to 15km and the dip to 45º W, following Biggs et al., (2010) and Ebinger et al., (2019). The

western side of the North Basin follows the edge of Mughese fault (Heilman et al., 2019) before connecting with the Karonga Fault. Although some models suggest the westward dipping St. Mary fault may be active (Biggs et al., 2010; Ebinger et al., 2019; Gaherty et al., 2019), I utilize the Karonga fault location because of the motion at the GPS site KARO (Figure 1). Located in Karonga, this site has a strong southeast velocity that suggests the site is not moving with either the Nubia or Rovuma blocks. If the St. Mary fault were used, KARO would be on Nubia. I follow Biggs et al., (2010) and Gaherty et al., (2019) in setting the dip at 60º E and a locking depth of 5 km for the Karonga Fault.

The Central Basin encompasses a series of alternating polarity border faults. Due to data distribution, I combine multiple faults into single boundaries as only the total deformation across the area can be constrained. On the west side, the model connects the Karonga fault with a model fault that is parallel but not coincident to the Usisya Fault (Accardo et al., 2018; Contreras et al., 2000; Laõ-Dávila et al., 2015) to better fit with the GPS velocity pattern. The model fault connects to the Bilila-Mtakataka bordering the southern edge of Lake Malawi (Jackson & Blenkinsop, 1997). Similar to the western border of the North Basin; these faults are set to a 5 km locking depth, based on seismic from Specht & Rosendahl, (1989), but have a dip of 70º E, determined by interpolating between the dips of determined in Williams et al., (2019). The southern segment of the Livingstone Fault (Accardo et al., 2018) is interpolated to connect with the Mbamba fault, a structure parallel to the Metangula fault, and Mwanjage fault (Flannery & Rosendahl, 1990; Rosendahl et al., 1992) as seen from North to South (Figure 10). These three western dipping faults share the same locking depths of 15 km and dips of 70º W, estimated and interpolated from seismic data (Specht & Rosendahl, 1989).

The South Basin consists primarily of the alternating polarity grabens that form the western edge of the model. The Bilila-Mtakataka fault terminates into the NW-SE Makanjira Graben, where the model boundary hugs the western edge of the graben. This graben truncates at the NNE-SSW Zomba Graben, before terminating into the NW-SE Lower Shire Graben (Lloyd et al., 2019; Williams et al., 2019). Each of these grabens dips between 45° and 70° (Williams et al., 2019), and locking depths are set to 5 km based on seismic interpretations (Laõ-Dávila et al., 2015; Specht and Rosendahl, 1989). The eastern border of the South Basin follows the trend of the Mwanjage border fault to Lake Chilwa where it connects to the Shire Graben by following topography.

4.3 A Priori Motion

The model allows for the inclusion of both *a priori* block motion estimates and fault slip rates. With the exception of a single *a priori* fault slip rate, I do not utilize either of these functions. All other Euler poles, angular velocities, and fault slip rates are a result of the inversion. The single *a priori* slip rate was used to constrain the dip-slip component of a section of the Chissenga Graben, where there is no GPS data. I utilize the relative motions of Saria et al., (2014) to constrain the fault plane motion to -3.0±0.5 mm/yr. In addition, I define the Nubian block to be fixed as it is the plate to which all motion is referenced. The definition of the Nubia plate will be discussed below.

4.4 Model Variations

In order to determine the model configuration for the Malawi Rift that best fits with the data, I compared a few different model configurations in addition to the preferred model discussed above. While many of the model configurations share the same general pattern, potential configurations around Malawi varied depending on which fault systems are interpreted to be the locus of extension. Each model was inverted with the same GPS data, solved via the same method, and was compared using the same statistics. Here I will briefly describe three alternate models. To compare each model, I utilize the weighted residual sum of squares statistic (WRSS). The preferred model has a WRSS value of 265.7.

4.4.1 Eastern Only Boundary

Examining the geology, GPS, and seismicity around the Malawi Rift lead to a few potential configurations. One possible configuration is that the steep border faults on the eastern side of Malawi accommodate the majority of the extension. This would be consistent with major geological features of the region, especially along the Livingstone, Mbamba, and Mwanjage border fault systems (Figure 10). In this model configuration the Mbamba and Mwanjage faults are connected in the model by a fault similar but not coincident with the Metangula border fault system. South of the Mwanjage system, I connect Lake Chilwa to the intersection of the Shire and Urema Grabens by following topography. This presents us with the configuration in Figure 11.

While this model fits well in some places, it fails to fully encapsulate the complexity of the region, particularly in terms of seismicity. With this model, there are no active boundaries near the ~M_w 6.0 2009 Karonga (Biggs et al., 2010) or the ~M_w 6.1 Salima-Dedza-Mchinji earthquakes (Hodge et al., 2015) which seems to be unlikely. The background seismicity (Figure 3) from the ISC Catalog (Engdahl et al., 2020; International Seismological Centre, 2020; Engdahl et al., 1998; Weston et al., 2018) also shows that while there is seismicity across the area, it is not equally distributed across the region. Instead, it is focused on roughly the center and west sides of the rift with a smaller but not insubstantial amount on the eastern border. This model has a WRSS value of 271.7.

4.4.2 Western Only Boundary

The second model configuration centers around the western boundary of Malawi. As discussed in the preferred model, the model connects to the Chisi/Ufipa and Usangu intersection via the Mughese fault, then follows the Karonga, Usisya, and Bilila-Mtakataka faults before connecting to the Zomba and Shire grabens (Figure 10; Figure 12). This boundary follows seismicity much better than the Eastern Only boundary as it aligns with the previous large earthquakes in Karonga and Salima-Dedza-Mchinji as well as background seismicity. With this configuration, it highlights the Bilila-Mtakataka fault, one of the segments with the potential for a M_w 8.0 earthquake (Jackson & Blenkinsop, 1997). However, this model does fail to adequately encapsulate the geology of the region. It leaves out the Livingstone Fault System, one of the most dominant features of the rift, as well as multiple well-defined border faults. This model has a WRSS value of 266.8.

4.4.3 Middle Boundary

The third model configuration follows the center of Lake Malawi through multiple fault systems. North of Malawi, the Chisi/Ufipa and Usangu intersection as the starting point, similar to the preferred model. The model connects to Lake Malawi via the Mughese fault (Heilman et al., 2019) before connecting with multiple North Basin faults running in the center of Lake Malawi identified in Mortimer et al., (2007). These faults connect with the north segment of the Central Border fault system identified in McCartney & Scholz, (2016) before connecting with a north-

south generalized Lipichili fault zone (Ebinger et al., 2019; McCartney & Scholz, 2016). The model extends the Lipichili to connect with the Metangula border fault system. The model connects the western edge of the Makanjira and Zomba Grabens near Lake Malawi before connecting with the Lower Shire Graben (Williams et al., 2019) and following the same path as the other alternate models.

This model configuration does fit with the ISC background seismicity, but it has similar potential problems with other models. It does not follow most of the well-defined border fault systems or align with major seismic events. It does, however, align well with multiple offshore faults better than the other alternate models. This model has a WRSS value of 265.9.

4.4.4 Preferred Model

The preferred model follows major border faults on each side of the lake. On the western boundary, it connects the Mughese fault (Heilman et al., 2019), Karonga (Biggs et al., 2010; Gaherty et al., 2019), Usisya (Accardo et al., 2018; Contreras et al., 2000; Laõ-Dávila et al., 2015), and Bilila-Mtakataka faults (Jackson & Blenkinsop, 1997; Specht & Rosendahl, 1989) before following the western edge of the Makanjira, Zomba, and Lower Shire Grabens (Lloyd et al., 2019; Williams et al., 2019). The Eastern boundary connects the Lupa (Heilman et al., 2019; Lavayssière et al., 2019; Lemna et al., 2019), Livingstone (Biggs et al., 2010; Ebinger et al., 2019; Accardo et al., 2018), Mbanmba, Metangula, and Mwanjage fault systems (Flannery & Rosendahl, 1990; Rosendahl et al., 1992) before connecting to the Shire Graben by following topography.

Multiple models have similar WRSS but seismic and geologic evidence suggest that a two fault system better describes the region. It is clear that there are well-defined border faults (e.g. Specht and Rosendahl, 1989; Ebinger et al., 2019; Williams et al., 2019) on both the sides of the rift that captures the alternating half graben system that is characteristic of the African Rift lakes. Seismicity in the region seems to be distributed across multiple fault systems on both sides of the lake (Ebinger et al., 2019). Although the largest earthquakes in the recorded history (e.g. Karonga, Salima-Dedza-Mchinji) seem to be located on the western boundary, it is clear that other fault systems (e.g. Livingstone, Metangula) have potential for large events (Hodge et al., 2015). In order to best incorporate the geology and seismicity of the region, I use the two border fault system as the preferred model.

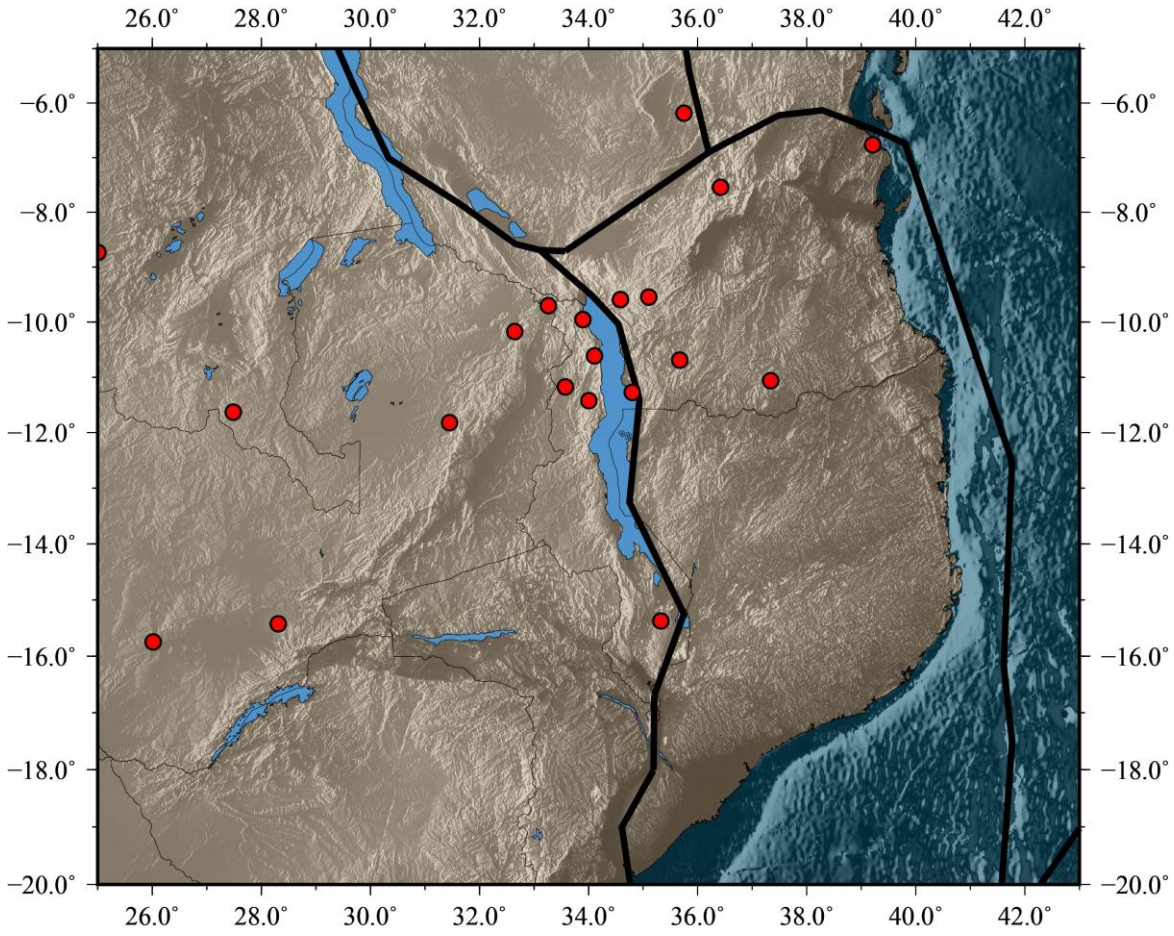

Figure 11 Configuration for the model with only an Eastern boundary. Red dots are GPS stations used in the model.

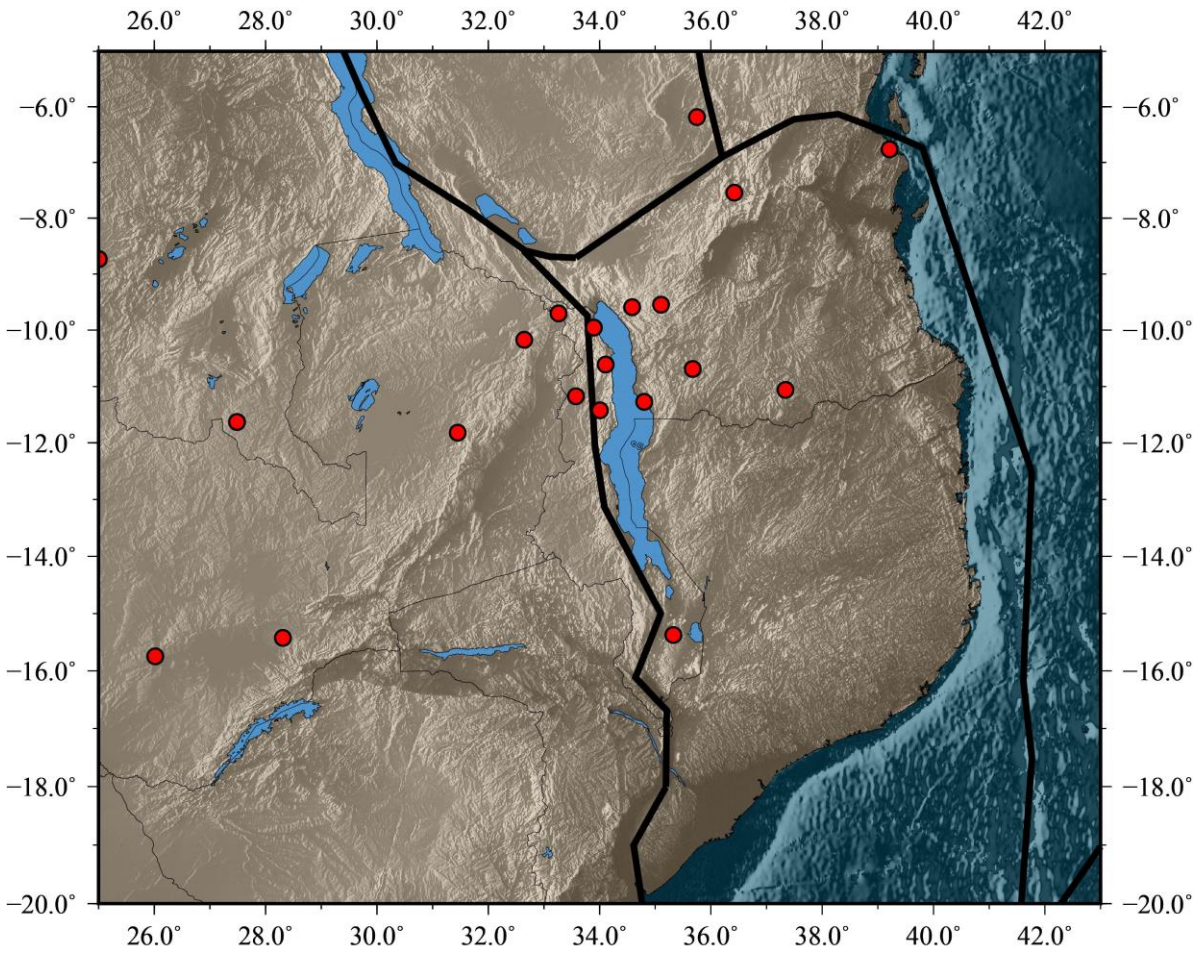

Figure 12 Configuration for the model with only a western boundary. Red dots are GPS stations used in the model.

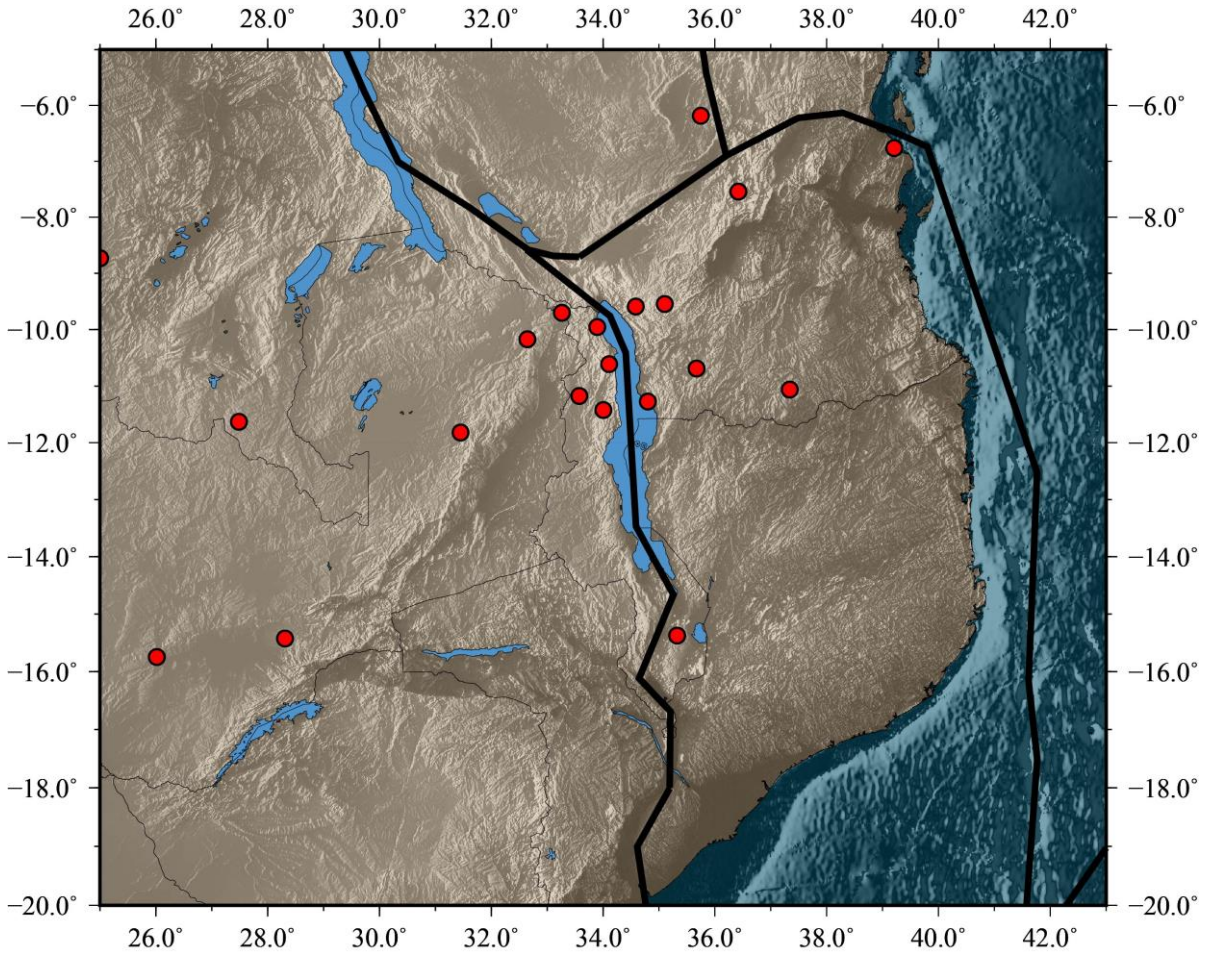

Figure 13 Configuration for the model with only a central boundary. Red dots are GPS stations used in the model.

5. RESULTS

5.1 Euler Poles and Angular Velocities

My dataset included 229 values (east and north components from 112 GPS sites and a slip rate constraint south of Malawi) in the inversion to estimate 30 parameters (Euler pole longitude, latitude, and rotation rate for 10 blocks). These parameters are presented in Table 2 with the exception of Nubia. As Nubia is the reference plate, it is defined to be stationary. Uncertainties for the poles in Table 2 are strongly affected by GPS data distribution. As data distribution is uneven (Figure 4-7), it is important to note that generally blocks with fewer number of sites tend to have higher uncertainties. A plot of the Euler poles for the preferred model (Figure 14) is discussed below.

The Antarctica plate pole is located northeast of Brazil between the Mid Atlantic Ridge and the coast (Figure 14). It is almost coincident with the Antarctic pole from Saria et al., (2014) and is similar to the pole of Stamps et al., (2008), each of which produce a clockwise rotation of the Antarctic plate similar to what is shown in the GPS (Figure 4) and models (Figure 15).

The Arabia pole is located near the center of the Mediterranean Sea. Close proximity of the pole to the block results in a very tight counterclockwise rotation. This plate has the highest rotation rate of any of the model blocks, and the large model velocities are consistent with GPS measurements, high slip rate faults (e.g. East Anatolian Fault Zone, Bulut et al., (2012)) and geologic features (e.g. Zagros Mountain Range).

The model Eurasia pole is located in the near the Mid Atlantic Ridge between Angola and Brazil (Figure 14). The location is outside the uncertainties of a more Eurasia focused model (e.g. Reilinger & McClusky, 2011). This is likely due to the more generalized boundaries used in the present model since the plate is far away from the focus area. The preferred model approximation with large generalizations of the northern boundary of Eurasia is adequate to explain observations at GPS sites across the Eurasian plate, which have similar clockwise rotation and magnitude (Figure 4).

The Somalia pole is located south-southwest from Madagascar in the center of the Lwandle plate. It is rotating slowly clockwise, with higher velocities present around the Main Ethiopian Rift as compared to the Somalia-Lwandle boundary. Previous studies have produced similar

motion rates with both geodetic (e.g. Fernandes et al., 2004; Saria et al., 2014) and geologic (e.g. Jestin et al., (1994)) data.

The Rovuma pole is also located on the Lwandle block, directly east of South Africa. This pole also rotates slowly clockwise but has a slightly slower rate than that of Somalia. The pole location is similar to that of Saria et al., (2014) and Stamps et al., (2008).

The preferred model differs from previous models when comparing both the Lwandle and Victoria poles. Even with very different pole locations, it is possible for different angular velocities to produce the same block motions. The model Lwandle pole is located slightly southeast of the plate, while Saria et al., (2014) and Stamps et al., (2008) are both located to the west, closer the Mid Atlantic Ridge. Their predicted velocities in the area are ~ 1 mm/yr, often within their error ellipses. The model velocities in this area are very small, consistent with a slowly rotating block (Figure 18; Figure 19). The Victoria pole is located near Greenland while both Saria et al., (2014) and Stamps et al., (2008) are near Sudan. The pole has a very high uncertainty in both the latitude and longitude, which may be because of the distortion during the nonlinear transformation from Cartesian to geographic coordinates at high latitudes (Elliott et al., 2010). However, while the pole is different, the predicted velocities in the area (Figure 15-17) are consistent with both data and other models.

As prior models have not included a Malawi block, the preferred solution is unique. The pole is located northeast of Malawi in Tanzania and is rotating slowly clockwise, resulting in higher velocities near the Zomba Graben (Figure 9; Figure 17; Figure 19) but consistent azimuths throughout the block.

Table 2 Euler Pole longitude, latitude, angular velocities, and associated uncertainties for blocks in the preferred model. Positive angular velocities correspond to clockwise motion. Uncertainties are 1-σ.

Plate	**Pole Long (°E)**	**Pole Lat (°N)**	**ω (deg/Ma)**	**σ_{Long}**	**σ_{Lat}**	**σ_{ω}**
Eurasia	168.020	7.729	0.058	1.948	4.837	0.003
Antarctica	139.048	-4.067	0.111	0.861	1.878	0.002
Arabia	18.689	33.128	0.339	1.792	0.472	0.017
Somalia	222.656	35.586	0.073	1.190	2.632	0.005
Victoria	356.418	73.885	0.027	195.137	74.615	0.008
Malawi	35.294	-5.815	0.066	2.314	5.925	0.061
Rovuma	220.796	28.710	0.059	2.083	1.553	0.010
Lwandle	225.984	47.189	0.033	9.887	90.063	0.103

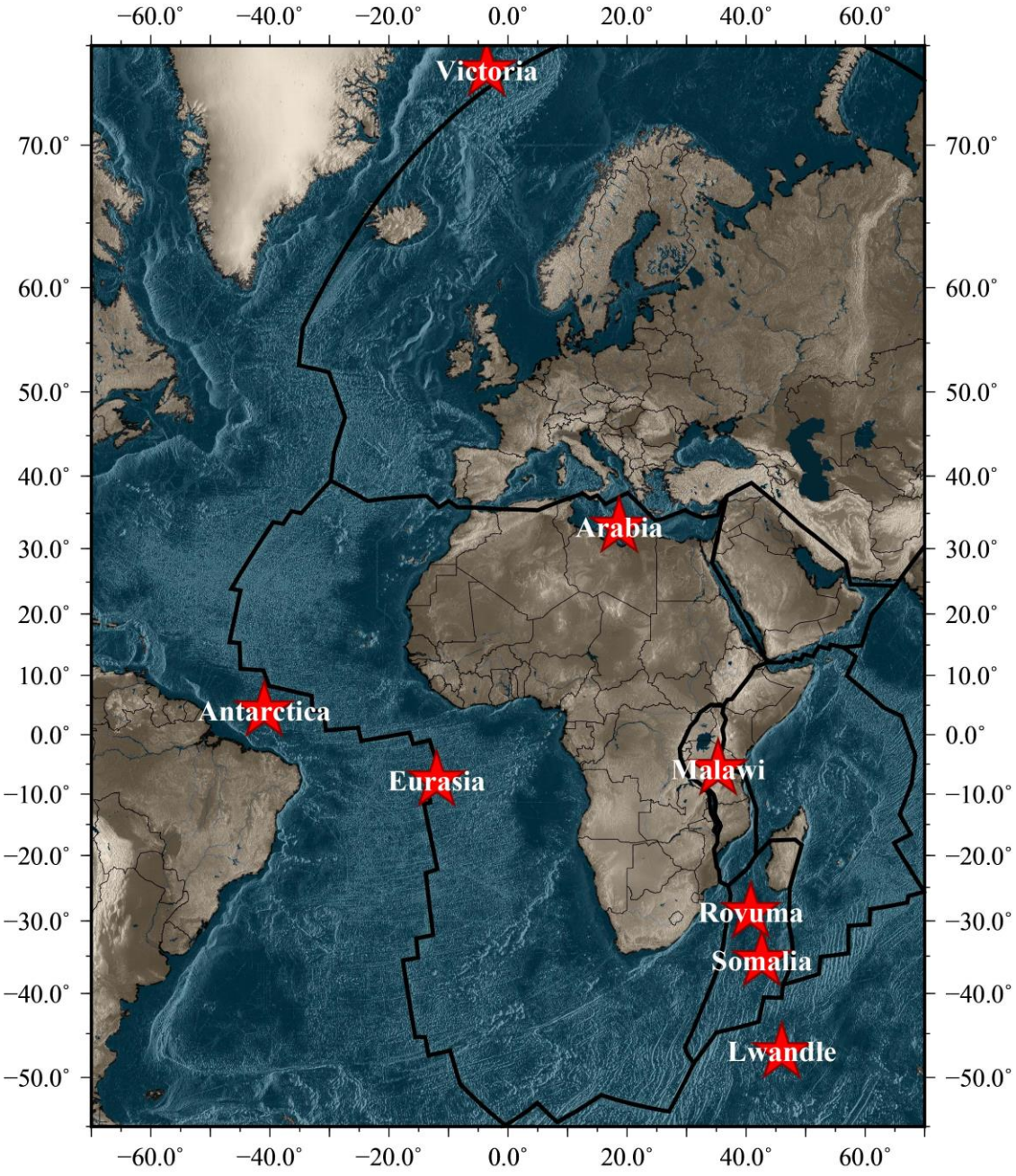

Figure 14 The location of all major Euler Poles for the preferred model. All poles are referenced to Nubia. Table 2 lists the coordinates, angular velocities, and uncertainties of each pole.

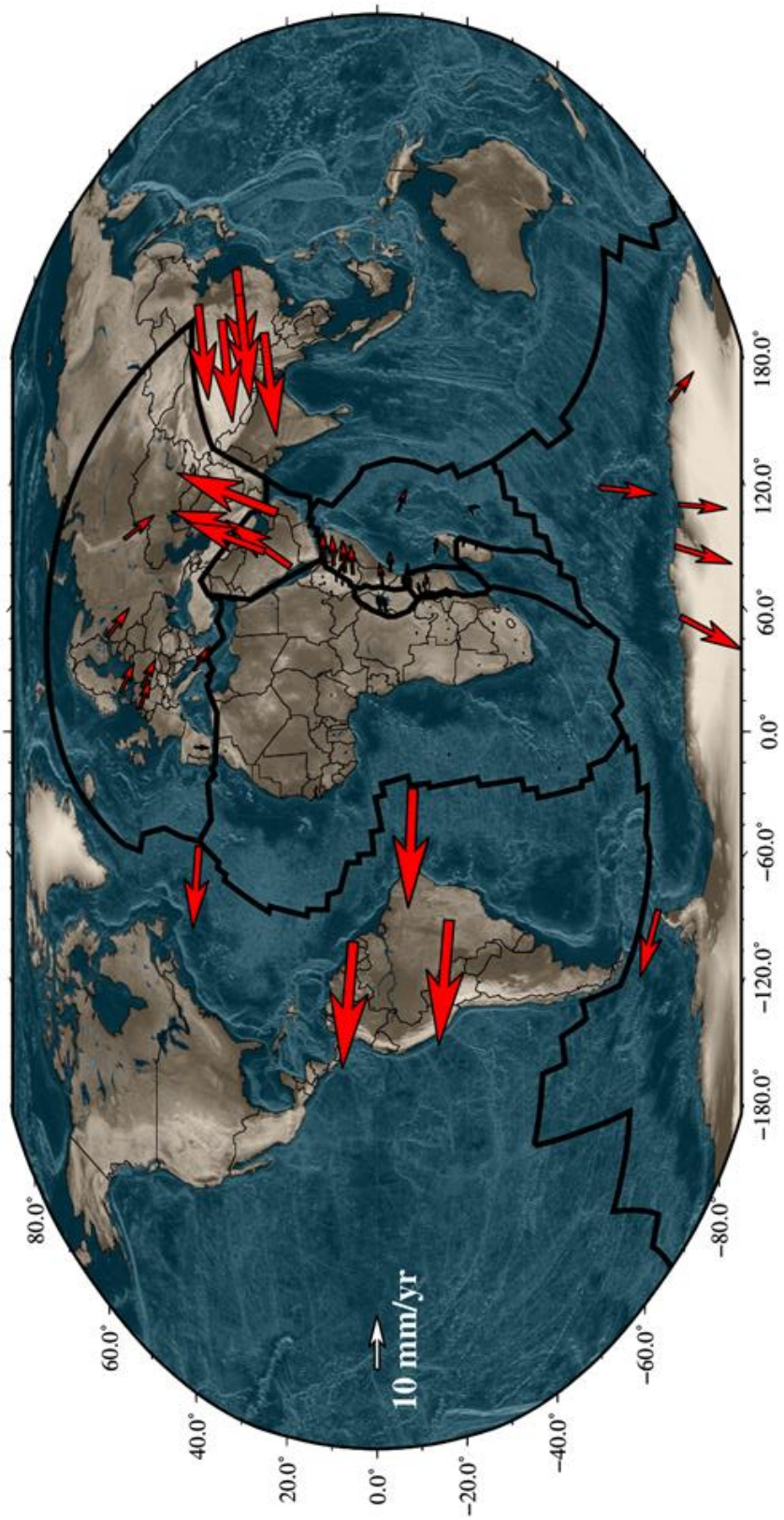

Figure 15 Preferred total model velocities at the global scale.

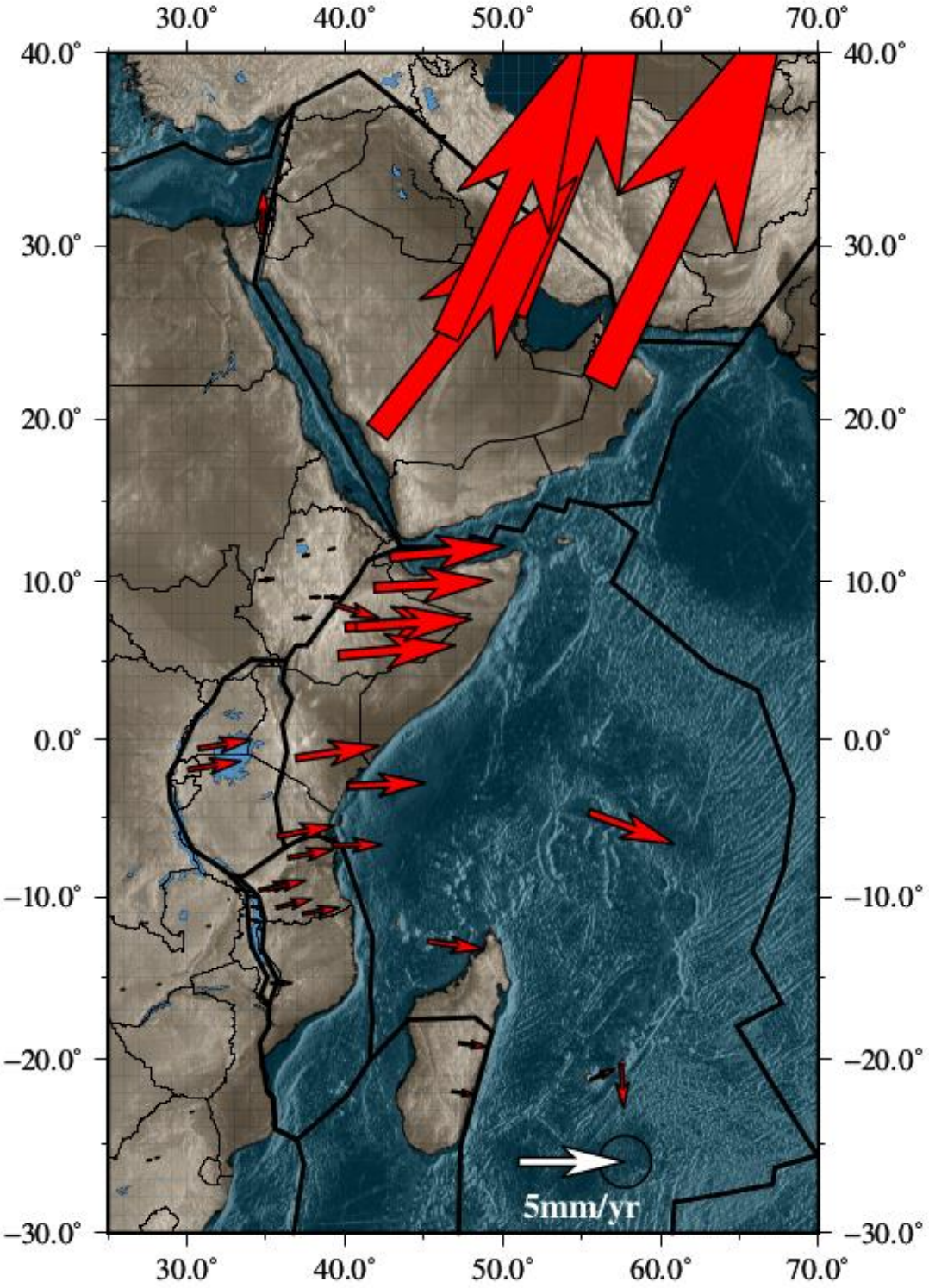

Figure 16 Preferred total model velocities for Malawi and surrounding plates.

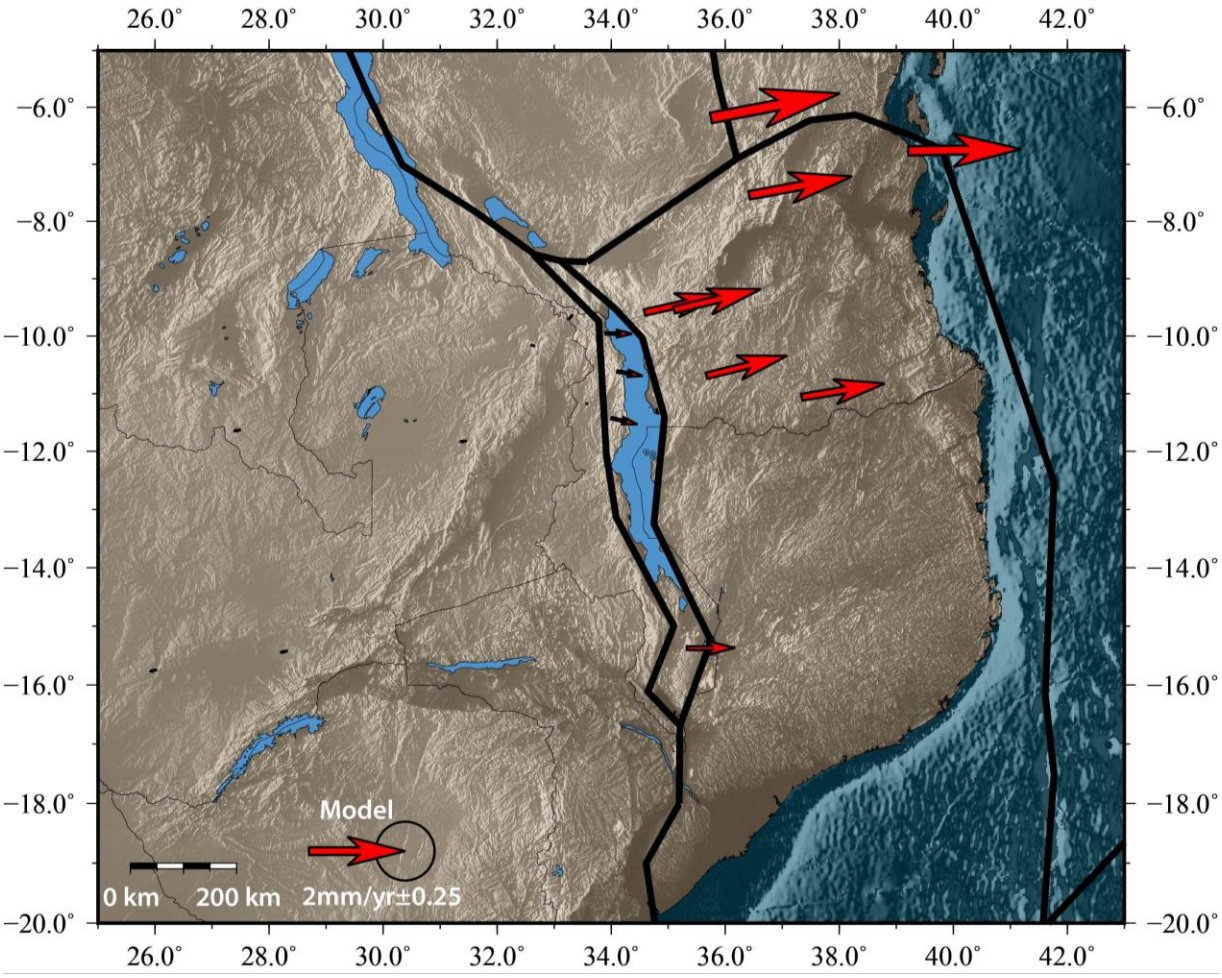

Figure 17 Preferred total model velocities near the Malawi Rift.

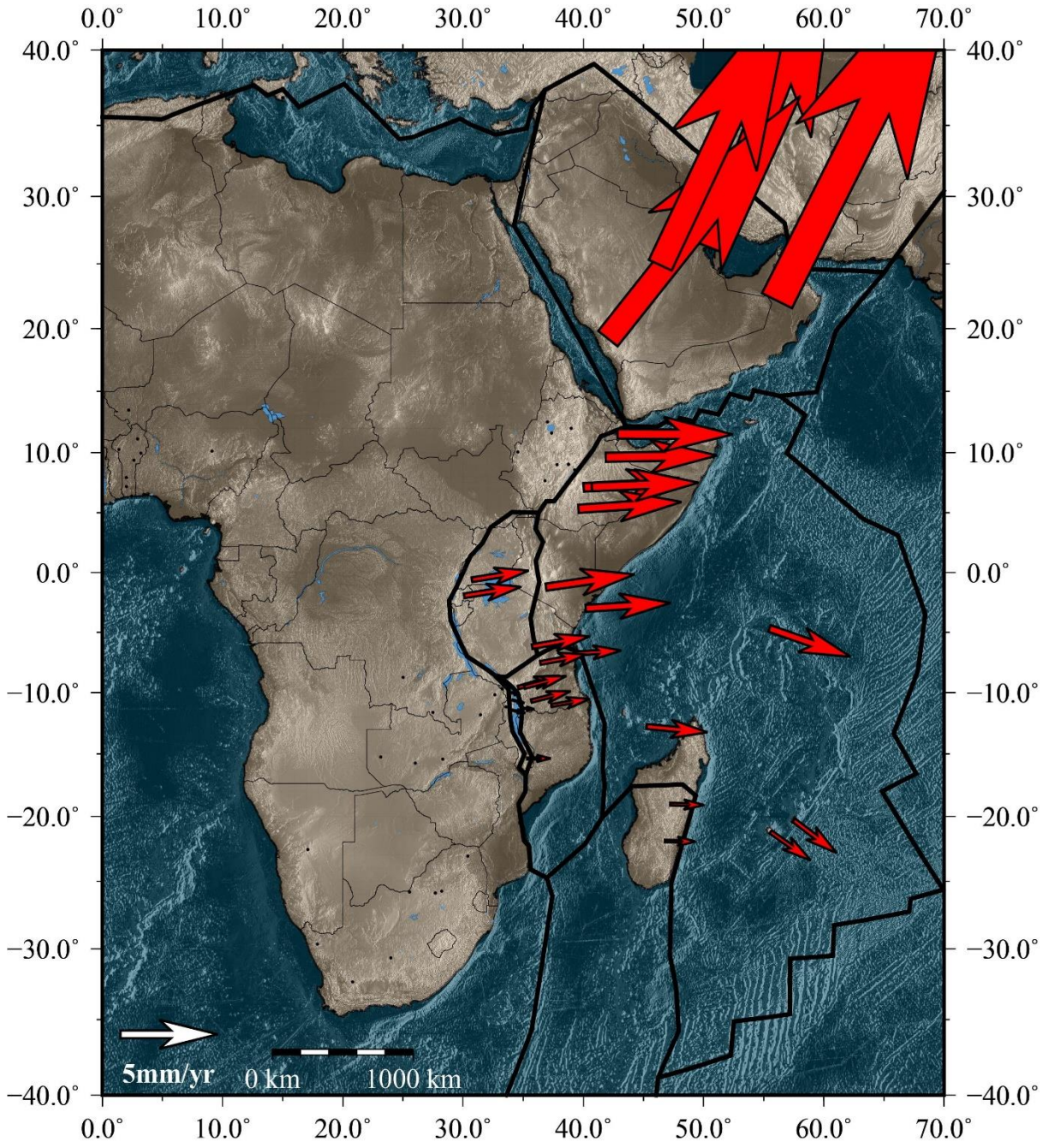

Figure 18 Rotational component of the preferred model velocities for areas around the East African Rift.

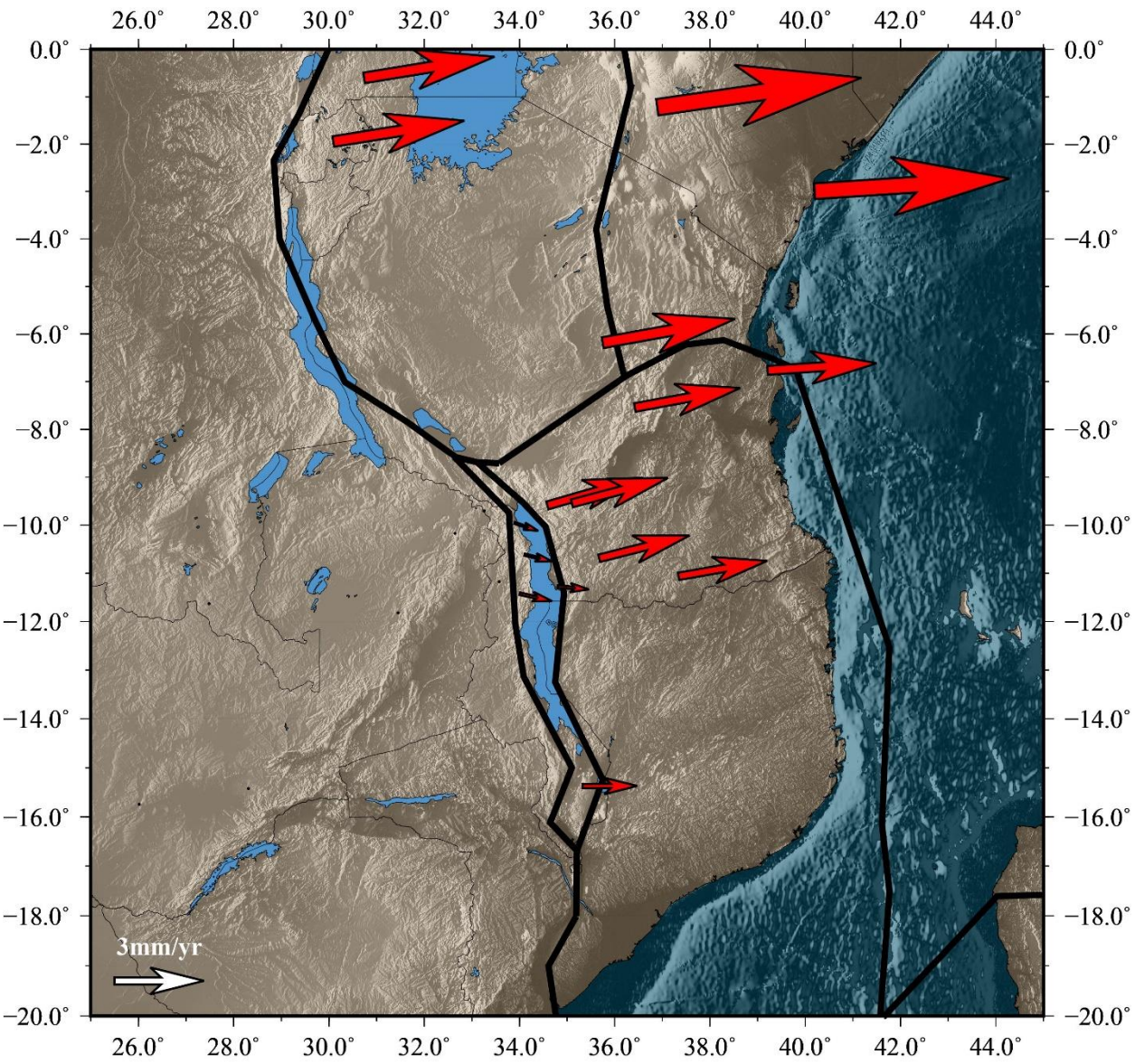

Figure 19 Rotational component of the preferred model velocities for areas around the Malawi Rift.

5.2 **Relative Block Motion Estimates**

Relative block motions calculated along the model boundaries are shown in Figure 20 and Figure 21. Predicted relative motions are comparable to previous models (e.g. Saria et al., (2014)) but have slightly different trends as discussed below. Extension is roughly balanced between the eastern and western rifts, with the western rift having a slightly higher rate of motion.

In the Eastern Branch near the Afar triple junction the Somalia plate is moving away from Nubia at ~6.0 mm/yr sinistral-oblique to the rift (Figure 20). This rate decreases to the southwest, following the Main Ethiopian Rift until it intersects the Western Branch. The western branch becomes then becomes the primary locus of extension, with rates staying roughly consistent with ~3mm/yr. As the trace of the rift changes from NE-SW to N-S the azimuth of the relative motions stays constant, becoming more perpendicular to the boundary. From the junction with the Western Rift at the North end of Victoria to the junction of Victoria and Rovuma in the south the relative motions slowly decrease from 2.2 mm/yr to 1.2 mm/yr.

The relative motions are significantly different from previous models (e.g. Saria et al., 2014; Stamps et al., 2008) around Malawi where the model complexity increases (Figure 21). In northern Malawi, most of the extension in the region is taken up along the Livingstone fault system to the east rather than the western branch of the rift system. This pattern continues as the rift propagates southward until the Metangula fault system, where the extension rates between the east and west sides of the rift are roughly even. In southern Malawi, the Zomba Graben is the locus of extension as opposed to the eastern boundary. Southern Malawi has roughly half the combined relative motion rate of that of the North Basin. Total extension rates across the North Basin are ~2.4 mm/yr slightly oblique to the strike of the Livingstone fault system; rates decrease to ~1.8 mm/yr in sinistral-oblique motion in the South Basin.

South of Malawi, relative motions decrease to ~1 mm/yr. Saria et al., (2014) and Stamps et al., (2008) both have predicted motions of ~1 mm/yr around the Lwandle block, but the direction varies with each model. Many of the values are within their uncertainty ellipse but the direction of motion is coherent across the region, suggesting a small reference frame error.

5.3 Goodness of Fit

Examining the preferred model residuals (Figure 22) reveals few discernable patterns. In Ethiopia, the residuals appear to be pointing away from the rift, suggesting that the model fails to capture some of the extension signal. The other location where there is a discernable pattern is in southern Africa, where some of the velocities trend northward with magnitudes < ~1 mm/yr. These residuals are almost entirely within their error ellipses. No patterns are discernable around the Malawi Rift (Figure 23).

The preferred model has a weighted residual sum of squares (WRSS) of 265.7. The mean residual magnitude is 2.2 mm/yr with roughly 32.9% of all residual being less than the mean 1-σ uncertainty.

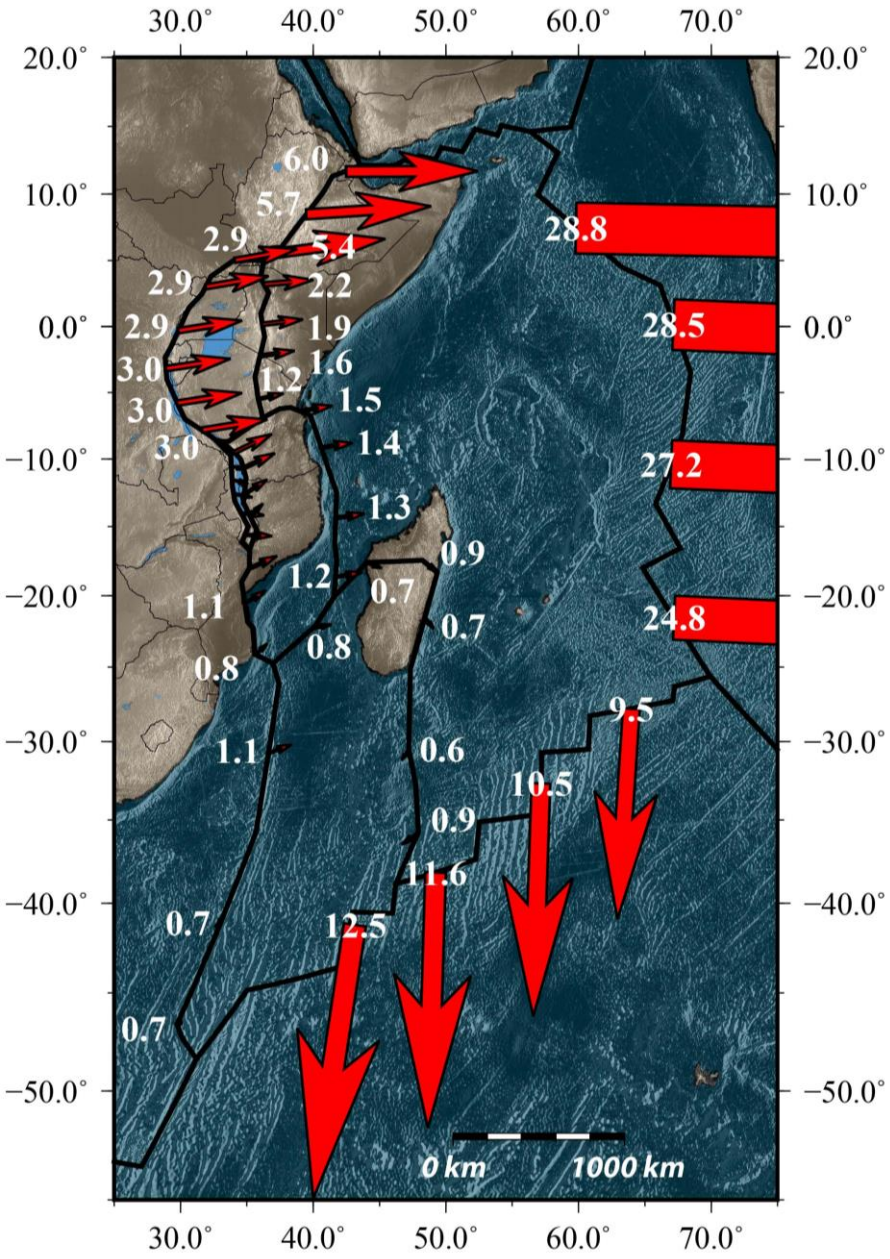

Figure 20 Predicted relative block motions for the preferred model at the scale of the East African Rift. The vectors and adjacent numbers represent the horizontal surface velocity in mm/yr between adjacent blocks.

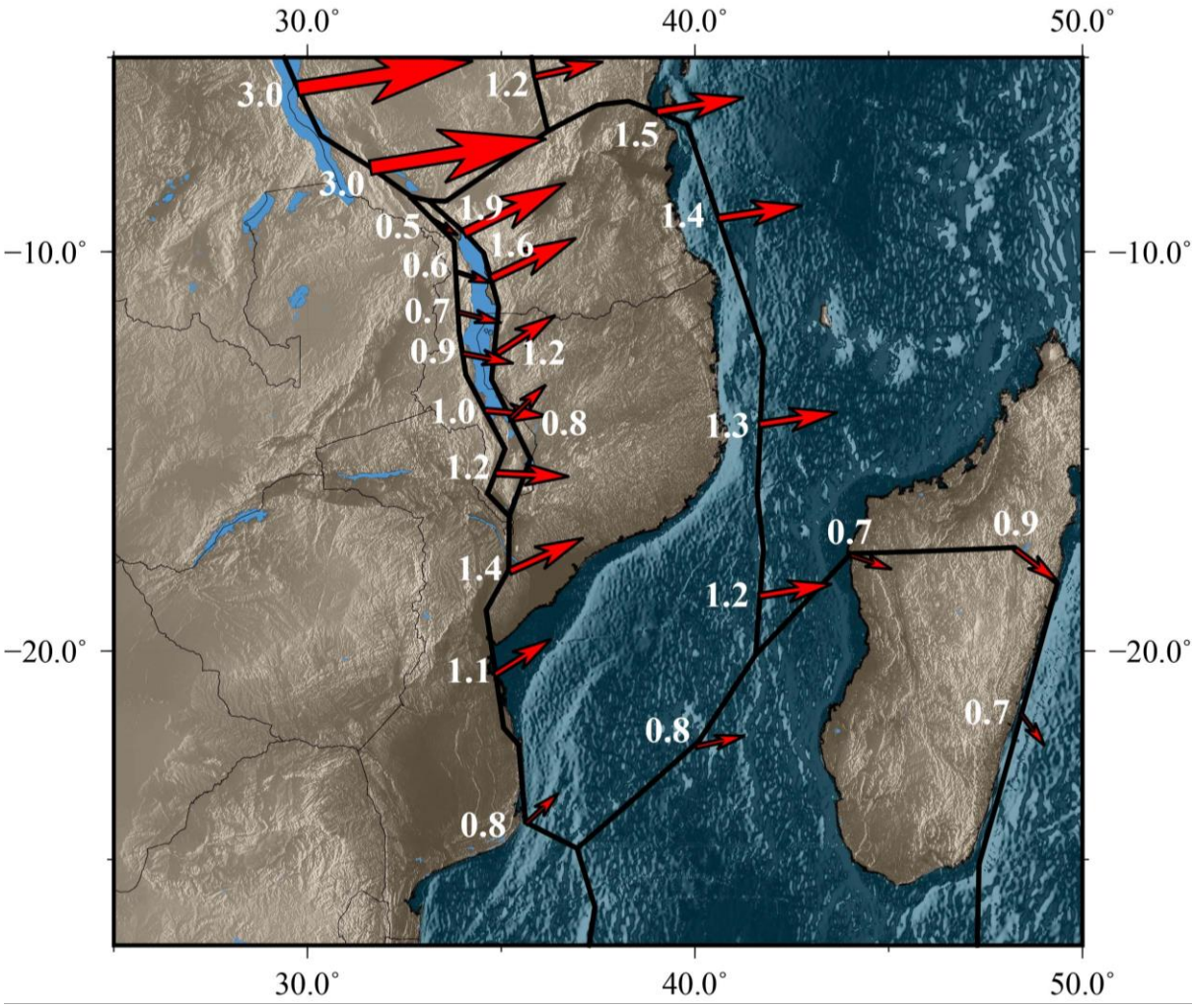

Figure 21 Predicted relative block motions for the preferred model for the area surrounding the Malawi Rift. The vectors and adjacent numbers represent the horizontal surface velocity in mm/yr between adjacent blocks.

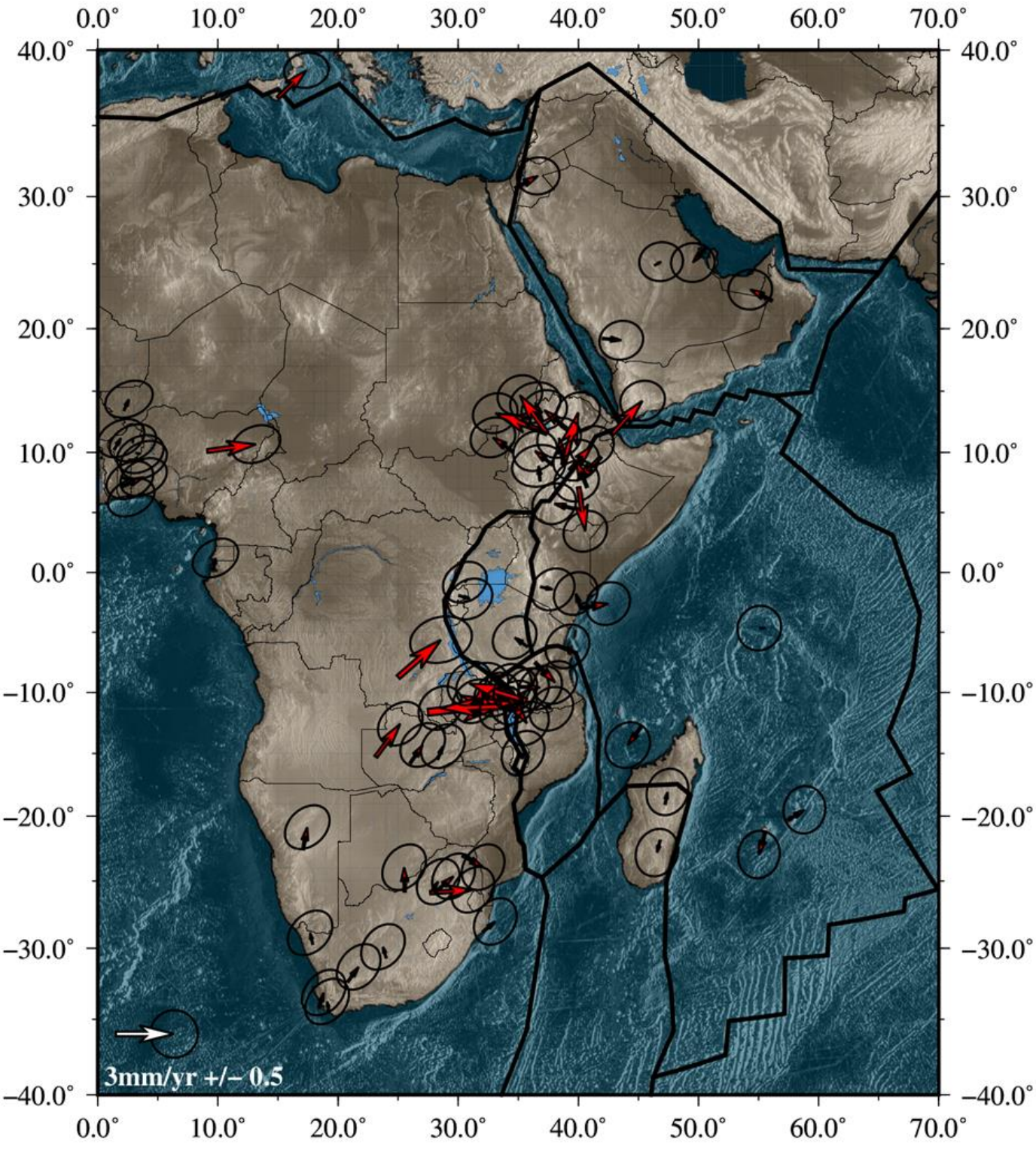

Figure 22 Preferred model residuals on the major plates surrounding the Malawi Rift.

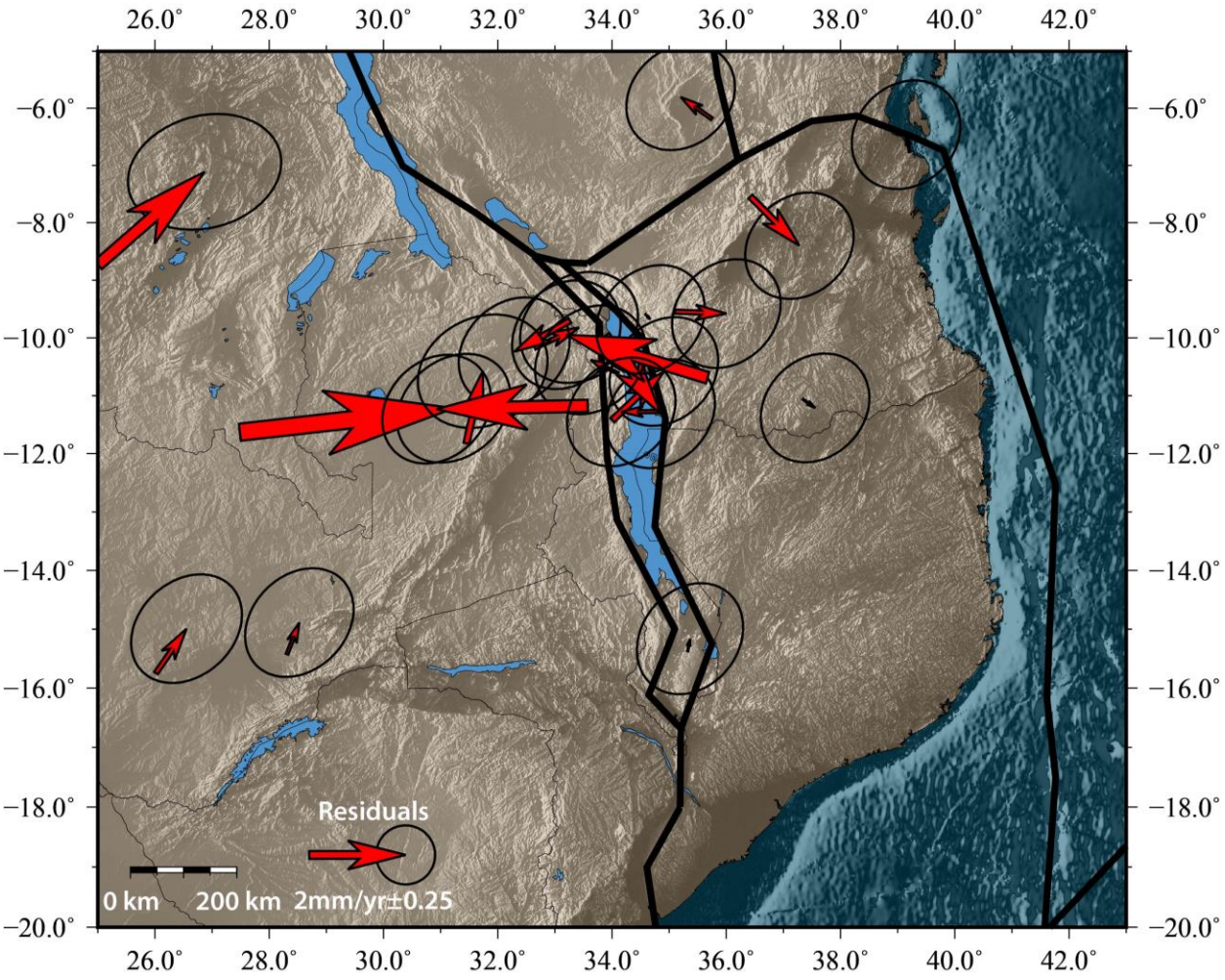

Figure 23 Preferred model residuals for the area surrounding the Malawi Rift.

6. DISCUSSION

6.1 Significance of the Malawi Block

The Malawi block is the smallest block in the model. As it follows the large boundary faults along the Rift, it is extremely elongated in one direction. The block itself is dominated by Lake Malawi, and therefore only has GPS sites along the edges. The sites that define the motion of the Malawi block do not display fully coherent block-like motion (Figure 7). These sites were put on the Malawi block due to location and the fact that their velocities do not fit with either those of sites on Rovuma or Nubia, which indicates that at least one additional block was needed. Two of these sites, KARO and MZUZ, have velocities outside their error ellipses with KARO pointing southeast and MZUZ pointing northeast. The velocity at ZOMB in southern Malawi has a similar orientation and magnitude to MZUZ but is on the same order of magnitude as its uncertainty ellipse. The two other sites used to define the Malawi block (MBBC and LIVA) are very small and within uncertainties; MBBC has a small westward component and LIVA is nearly zero. When modeled, the motion at these sites is primarily from the rotation of the Malawi Block. MBBC is an exception as it has elastic strain and block motion that are similar in magnitude and direction (Figure 17; Figure 19).

Examining the statistics for the primary and alternate models suggests that I am currently unable to determine if the preferred model is statistically better than any of the three alternate models if I rely only on the current GPS dataset. Model choice, can, however, be justified through other datasets. The other primary geophysical dataset available is seismic. Data from Project PROBE (Scholz et al., 1989) and the SEGMeNT project (Shillington et al., 2016) have been used to interpret the subsurface (e.g Specht & Rosendahl, 1989; Shillington et al., 2020, respectively) to identify the location, depth and orientations of faults that would be impossible to characterize by geodetic data alone. These datasets suggest that deformation is happening both on the large border faults and on intrabasin faults (Biggs et al., 2010; Ebinger et al., 2019; McCartney & Scholz, 2016; Shillington et al., 2020), agreeing with the seismicity in the area (Figure 3) and further justifying the use of two border faults.

Fully describing the deformation around the Malawi Rift will require a longer time span of GPS data. With such slow extension rates the length of time that the GPS are actively recording is crucial. Longer active times reduce the uncertainty and lead to more robust velocities.

6.2 Seismic Hazards

While the extension rate in the region is low, there is still potential for large earthquakes. Three large earthquakes (Figure 3) have happened in recorded history: the 2009 M_w 5.9 Karonga Earthquake, the 1989 M_w 6.1 Salima-Dedza-Mchinji Earthquake, and the 1910 M_s 7.4 Rukwa Earthquake (Biggs et al., 2010; Hodge et al., 2015). While the Karonga and Salima-Dedza-Mchinji earthquakes are well located, the 1910 Rukwa earthquake was only recorded by instruments in Europe as there were no local seismometers at the time. Therefore, location estimates for this earthquake are poor (Ambraseys & Adams, 1991).

While these earthquakes were significant, the Malawi Rift has potential for larger events as well. Based on the probabilistic seismic hazard analysis (PSHA) calculations of Hodge et al., (2015), there is potential for up to an M_w 8.3 along the Metangula fault system at a recurrence interval of 2,600 years. Most other fault systems in the area, if they rupture as a single event, are capable of producing up to M_w ~7.5 to M_w ~8.0 at recurrence intervals of 2,300-4,300 years. However, the Livingstone fault system could produce up to an M_w 8.0 at a much shorter interval of 1,000 years. One of the inputs for this model was the motion estimates from Stamps et al., (2008) at a rate of 3.8 ± 0.7 mm/yr, substantially higher than my model estimate of 1.7 ± 0.4 mm/yr. The Stamps et al., (2008) model used a single fault in Malawi as opposed to the double fault geometry, but even with the dip-slip motion from both the Karonga (0.65 ± 0.25 mm/yr) and Livingstone (1.7 ± 0.4 mm/yr) fault segments combined into a single estimate, my model yields a much smaller total rate (2.35 ± 0.65 mm/yr) than predicted by previous models. This trend of decreased motion rates compared to previous studies continues as the Rift propagates southward, reaching a minimum of 1.26 ± 0.85 mm/yr in the Shire Graben.

To examine the effect of smaller extension rates on seismic hazard estimates, I recalculate the recurrence interval for two major fault systems using the methods of Hodge et al., (2015). Assuming that the faults rupture as one large segment and that the magnitudes of the earthquakes are the same as previously estimated, we calculate that a M_w ~7.8 event on the Livingstone fault

system has a recurrence interval of ~2,000 years, double the previous estimate of Hodge et al., (2015). For the Metangula fault system, previous estimates calculate a recurrence interval of ~2,600 years for a M_w ~8.1 event but using my smaller motion rates I calculate an interval of ~8,000 years. Although seismic hazard estimates can be heavily influenced by motion rates along plate boundaries, fault geometries and modeling techniques may also impact estimates. A more detailed comparison study with updated fault geometries based on seismic data would improve the estimates.

6.3 Discrete Vs Distributed Deformation

Block modeling requires defining discrete faults to create blocks. Discrete faults, however, do not always fully describe deformation in the area. Some block boundaries are simplifications of complex fault zones. Other regions (e.g Afar) can have distributed deformation that cannot be fully described by discrete faults.

To investigate possible distributed deformation in the Malawi Rift, I first analyze how the seismicity of the region compares with the block boundaries (Figure 3; Figure 10) to examine if discrete deformation is able to adequately describe deformation patterns in the region. Although errors in earthquake locations can be large (Gaherty et al., 2019; Weston et al., 2018), the seismicity and the eastern model boundary of the Malawi Block align well with the eastern edge of Lake Malawi. Near the Metangula fault system, seismicity is concentrated near the lake shore with only scattered events on land. Similarly, the Mwanjage fault system has clusters of seismicity along the northern section of the fault but the total amount of earthquakes decreases towards the southeastern end of the fault. Along the western model boundary, the amount of seismicity increases drastically compared to the eastern boundary. Lines of localized seismicity follow the Mughese Shear Zone until it connects with the Karonga Fault. The 2009 Karonga cluster of earthquakes occurs onshore, resulting in a dense cloud of seismicity centered around the four major events (Biggs et al., 2010; Ebinger et al., 2019; Hodge et al., 2015). Clusters of seismicity follow the lakeshore, coincident with the Usisya and Bilila-Mtakataka fault systems. Another large group of earthquakes occurs around the 1989 Salima-Dedza-Mchinji events, just north of the Bilila-Mtakataka fault system. South of Lake Malawi near the Zomba Graben, seismicity becomes less clustered but increases in quantity again in the Urema and Chissenga Grabens.

Although the border faults have localized seismicity around them, off border fault seismicity does occur within Lake Malawi and the surrounding area. In the North Basin of Lake Malawi, the updated seismicity mapped in Ebinger et al., (2019) shows clusters of earthquakes that occur on a series of intrabasin faults mapped in Mortimer et al., (2007). In the Central Basin, seismicity occurs on a sequence of intrabasin faults but is distributed across a wide area (Ebinger et al., 2019; McCartney & Scholz, 2016). The South Basin is also populated with off boundary fault seismicity with a large cluster being centered far south of the lake. West of Lake Malawi, seismicity is scattered over a large area but is abundant. Diffuse, low magnitude seismicity covers the entire area west of the border faults past the Luangwa Rift but is only poorly associated with structures. East of Lake Malawi, seismicity is very sparse and does not outline any large-scale structures.

The diffuse seismicity around Lake Malawi (Figure 3) suggest that deformation is not fully localized on a few, major fault systems. On the eastern boundary, seismicity does seem to be localized on some of the border faults but more diffuse seismicity to the east of the border fault cannot be described by a major border fault system. The western boundary does have large clusters of seismicity around the major faults, but seismicity extends past the border faults. While the preferred model boundaries are generalizations of multiple fault systems, it is clear that not all deformation can accurately be described purely by these discrete fault systems. Comparing the residual velocities (Figure 23) to the seismicity (Figure 2; Figure 3) yields interesting results. In the Rovuma block, intrablock seismicity is sparse and residuals are small, suggesting that the region behaves in a rigid block-like manner. West of Karonga, where the model residuals are larger, corresponds to diffuse seismicity suggesting that the region does not behave like a rigid block and that distributed deformation plays a larger role.

6.4 **Bangweulu Block**

The Bangweulu block is an area of thickened lithosphere southwest of Lake Tanganyika (Andersen & Unrug, 1984). While many geophysical models (e.g. Lavayssière et al., 2019; Njinju et al., 2019; O'Donnell et al., 2013) suggest that the Bangweulu block is a discrete lithospheric block, I do not include it in any of the models. Examining the GPS data (Figure 4; Figure 6) reveals no patterns in the data that suggest an additional block inside the Nubian craton is required. The

majority of the vectors on the Bangweulu block are very small, indicating they are likely on the Nubia plate. There few large vectors have no coherent spatial pattern to suggest that there is signal other than random noise.

CONCLUSIONS

I use data from 114 GPS sites, including 12 new sites in Tanzania, Malawi, and Zambia to create a block model of the Malawi Rift in order to examine deformation and extension rates. Integrating GPS, seismic, and geologic data surrounding the Malawi Rift suggests that an independent Malawi Plate may be required, shedding new light on rifting processes along the immature Malawi Rift. Results from the model show that while there is localized strain on border faults, distributed strain may also be required. The relative motions calculated are smaller than previously published extension rates around the Malawi Rift, varying from 2.35 ± 0.65 mm/yr in the North Basin to 1.26 ± 0.85 mm/yr in southern Malawi. Given the smaller extension rates, I suggest that recurrence intervals for major fault systems are much larger than previously estimated.

APPENDIX A. GPS DATA CITATIONS

Table A.1 DOI and References for GPS sites

Site Name	DOI	Reference
ABOO	10.7283/T5QJ7F71	Bendick, Rebecca, 2013, Ethiopia Tectonics GPS Network: ABOO-AMBO P.S., UNAVCO, GPS Data Set, doi:10.7283/T5QJ7F71
ASOS	10.7283/T55H7D6V	Bendick, Rebecca, 2013, Ethiopia Tectonics GPS Network: ASOS-Assosa P.S., UNAVCO, GPS Data Set, doi:10.7283/T55H7D6V
BDAR	10.7283/T5TB14TH	Bendick, Rebecca and Reilinger, Robert E., 2007, Ethiopia Tectonics GPS Network: BDAR-Bahir Dar P.S., UNAVCO, GPS Data Set, doi:10.7283/T5TB14TH
BDMT	10.7283/T52R3PMH	Bendick, Rebecca, 2013, Ethiopia Tectonics GPS Network - BDMT-Bahir Dar P.S., The GAGE Facility operated by UNAVCO, Inc., GPS/GNSS Observations Dataset, https://doi.org/10.7283/T52R3PMH.
CTPM	10.7283/T5J38QW6	Nooner, Scott, Ebinger, Cynthia J., Saria, Elifuraha, Chindandali, Patrick, Ntambila, Daud, Shillington, Donna J., Pritchard, Matt, Elliott, Julie L., Nyblade, Andy, 2013, Malawi Rifting GPS Network, The GAGE Facility operated by UNAVCO, Inc., GPS/GNSS Observations (Aggregation of Multiple Datasets), https://doi.org/10.7283/T5J38QW6.
DAKA	10.7283/T5JH3JG0	Savage, James C., 1999, Alaska USGS 1993, UNAVCO, GPS Data Set, doi:10.7283/T5JH3JG0
DODM	10.7283/T5319SZK	Nyblade, Andy, 2010, Africa Array GPS Network: DODM-Entebbe P.S., UNAVCO, GPS Data Set, doi:10.7283/T5319SZK
GINR	10.7283/T5KS6PH9	Bendick, Rebecca, 2013, Ethiopia Tectonics GPS Network: GINR-Ginir P.S., UNAVCO, GPS Data Set, doi:10.7283/T5KS6PH9
IFRN	10.7283/T5C24TPB	Ben Sari, Driss, Fadil, Abdelali and Reilinger, Robert E., 2001, Morocco Continuous GPS Stations: Ifran Morocco Continuous GPS Station (IFRN), UNAVCO, GPS Data Set, doi:10.7283/T5C24TPB

Site Name	DOI	Reference
ISOK	10.7283/T5J38QW6	Nooner, Scott, Ebinger, Cynthia J., Saria, Elifuraha, Chindandali, Patrick, Ntambila, Daud, Shillington, Donna J., Pritchard, Matt, Elliott, Julie L., Nyblade, Andy, 2013, Malawi Rifting GPS Network, The GAGE Facility operated by UNAVCO, Inc., GPS/GNSS Observations (Aggregation of Multiple Datasets), https://doi.org/10.7283/T5J38QW6.
KARO	10.7283/T5J38QW6	Nooner, Scott, Ebinger, Cynthia J., Saria, Elifuraha, Chindandali, Patrick, Ntambila, Daud, Shillington, Donna J., Pritchard, Matt, Elliott, Julie L., Nyblade, Andy, 2013, Malawi Rifting GPS Network, The GAGE Facility operated by UNAVCO, Inc., GPS/GNSS Observations (Aggregation of Multiple Datasets), https://doi.org/10.7283/T5J38QW6.
KFNY	10.7283/T5J38QW6	Nooner, Scott, Ebinger, Cynthia J., Saria, Elifuraha, Chindandali, Patrick, Ntambila, Daud, Shillington, Donna J., Pritchard, Matt, Elliott, Julie L., Nyblade, Andy, 2013, Malawi Rifting GPS Network, The GAGE Facility operated by UNAVCO, Inc., GPS/GNSS Observations (Aggregation of Multiple Datasets), https://doi.org/10.7283/T5J38QW6.
LIVA	10.7283/T5J38QW6	Nooner, Scott, Ebinger, Cynthia J., Saria, Elifuraha, Chindandali, Patrick, Ntambila, Daud, Shillington, Donna J., Pritchard, Matt, Elliott, Julie L., Nyblade, Andy, 2013, Malawi Rifting GPS Network, The GAGE Facility operated by UNAVCO, Inc., GPS/GNSS Observations (Aggregation of Multiple Datasets), https://doi.org/10.7283/T5J38QW6.
MALI	10.7283/T5B8568N	Bock, Yehuda, Subarya, Cecep, McCaffrey, Rob, 1999, Indonesia 1997, The GAGE Facility operated by UNAVCO, Inc., GPS/GNSS Observations Dataset, https://doi.org/10.7283/T5B8568N.

Site Name	DOI	Reference
MATL	10.7283/T5J38QW6	Nooner, Scott, Ebinger, Cynthia J., Saria, Elifuraha, Chindandali, Patrick, Ntambila, Daud, Shillington, Donna J., Pritchard, Matt, Elliott, Julie L., Nyblade, Andy, 2013, Malawi Rifting GPS Network, The GAGE Facility operated by UNAVCO, Inc., GPS/GNSS Observations (Aggregation of Multiple Datasets), https://doi.org/10.7283/T5J38QW6.
MBBC	10.7283/T5J38QW6	Nooner, Scott, Ebinger, Cynthia J., Saria, Elifuraha, Chindandali, Patrick, Ntambila, Daud, Shillington, Donna J., Pritchard, Matt, Elliott, Julie L., Nyblade, Andy, 2013, Malawi Rifting GPS Network, The GAGE Facility operated by UNAVCO, Inc., GPS/GNSS Observations (Aggregation of Multiple Datasets), https://doi.org/10.7283/T5J38QW6.
MONG	10.7283/T57S7KVT	Nyblade, Andy, 2011, Africa Array GPS Network: MONG-Mongu P.S., UNAVCO, GPS Data Set, doi:10.7283/T57S7KVT
MPIK	10.7283/T5J38QW6	Nooner, Scott, Ebinger, Cynthia J., Saria, Elifuraha, Chindandali, Patrick, Ntambila, Daud, Shillington, Donna J., Pritchard, Matt, Elliott, Julie L., Nyblade, Andy, 2013, Malawi Rifting GPS Network, The GAGE Facility operated by UNAVCO, Inc., GPS/GNSS Observations (Aggregation of Multiple Datasets), https://doi.org/10.7283/T5J38QW6.
MTDK	10.7283/T5J38QW6	Nooner, Scott, Ebinger, Cynthia J., Saria, Elifuraha, Chindandali, Patrick, Ntambila, Daud, Shillington, Donna J., Pritchard, Matt, Elliott, Julie L., Nyblade, Andy, 2013, Malawi Rifting GPS Network, The GAGE Facility operated by UNAVCO, Inc., GPS/GNSS Observations (Aggregation of Multiple Datasets), https://doi.org/10.7283/T5J38QW6.
MZUZ	10.7283/T5GB225F	Nyblade, Andy, 2010, Africa Array GPS Network: MZUZ-Mzuzu P.S., UNAVCO, GPS Data Set, doi:10.7283/T5GB225F

Site Name	DOI	Reference
NAZR	10.7283/T5F18WNH	Bendick, Rebecca and Reilinger, Robert E., 2007, Ethiopia Tectonics GPS Network: NAZR-Nazret P.S., UNAVCO, GPS Data Set, doi:10.7283/T5F18WNH
NEGE	10.7283/T5B8562Z	Bendick, Rebecca, 2013, Ethiopia Tectonics GPS Network: NEGE-Negele P.S., UNAVCO, GPS Data Set, doi:10.7283/T5B8562Z
RABT	10.7283/T53J3B67	Ben Sari, Driss, Ouazar, Driss, Fadil, Abdelali, Koulali, Achraf and Reilinger, Robert E., 2000, GGN GPS Network: Rabat Morocco Continuous GPS Station (RABT), UNAVCO, GPS Data Set, doi:10.7283/T53J3B67
ROBE	10.7283/T5G15XSW	Bendick, Rebecca and Reilinger, Robert E., 2007, Ethiopia Tectonics GPS Network: ROBE-Robe P.S., UNAVCO, GPS Data Set, doi:10.7283/T5G15XSW
SERB	10.7283/T56H4FB7	Bendick, Rebecca, 2013, Ethiopia Tectonics GPS Network: SERB-Seraba P.S., UNAVCO, GPS Data Set, doi:10.7283/T56H4FB7
SHIS	10.7283/T5JS9NCX	Bendick, Rebecca, 2013, Ethiopia Tectonics GPS Network: SHIS-Shimsheha P.S., UNAVCO, GPS Data Set, doi:10.7283/T5JS9NCX
SNGC	10.7283/T5J38QW6	Nooner, Scott, Ebinger, Cynthia J., Saria, Elifuraha, Chindandali, Patrick, Ntambila, Daud, Shillington, Donna J., Pritchard, Matt, Elliott, Julie L., Nyblade, Andy, 2013, Malawi Rifting GPS Network, The GAGE Facility operated by UNAVCO, Inc., GPS/GNSS Observations (Aggregation of Multiple Datasets), https://doi.org/10.7283/T5J38QW6.

Site Name	DOI	Reference
TAMA	10.7283/T5KK9920 10.7283/T5V40SF9 10.7283/T5QC01RD	Reilinger, Robert E., Gonzalez, Javier, Larsen, Shawn, Bennett, Rick, Bevis, Michael, Hudnut, Kenneth, Gilbert, Lewis, Beavan, John, Feaux, Karl, Jackson, Michael, Stowell, James, 1999, S. California, N. Baja Mexico MIT GPS Campaigns - 1989, The GAGE Facility operated by UNAVCO, Inc., GPS/GNSS Observations Dataset, https://doi.org/10.7283/T5QC01RD. Reilinger, Robert E., Gonzalez, Javier, Larsen, Shawn, Bennett, Rick, Bevis, Michael, Hudnut, Kenneth, Gilbert, Lewis, Beavan, John, Feaux, Karl, Jackson, Michael, Stowell, James, 1998, S. California, N. Baja Mexico MIT GPS Campaigns - 1986, The GAGE Facility operated by UNAVCO, Inc., GPS/GNSS Observations Dataset, https://doi.org/10.7283/T5V40SF9. Reilinger, Robert E., Gonzalez, Javier, Larsen, Shawn, Bennett, Rick, Bevis, Michael, Hudnut, Kenneth, Gilbert, Lewis, Beavan, John, Feaux, Karl, Jackson, Michael, Stowell, James, 1999, S. California, N. Baja Mexico MIT GPS Campaigns - 1990, The GAGE Facility operated by UNAVCO, Inc., GPS/GNSS Observations Dataset, https://doi.org/10.7283/T5KK9920.
TEZI	10.7283/T5QR4V6G	Nyblade, Andy, 2011, Africa Array GPS Network: TEZI-Itezi-Tezi P.S., UNAVCO, GPS Data Set, doi:10.7283/T5QR4V6G
TNDC	10.7283/T5J38QW6	Nooner, Scott, Ebinger, Cynthia J., Saria, Elifuraha, Chindandali, Patrick, Ntambila, Daud, Shillington, Donna J., Pritchard, Matt, Elliott, Julie L., Nyblade, Andy, 2013, Malawi Rifting GPS Network, The GAGE Facility operated by UNAVCO, Inc., GPS/GNSS Observations (Aggregation of Multiple Datasets), https://doi.org/10.7283/T5J38QW6.
UKAM	10.7283/T57D2SCB	Delvaux, Damien, 2010, Africa Array GPS Network: UKAM-UNIKAM P.S., UNAVCO, GPS Data Set, doi:10.7283/T57D2SCB
ULUB	10.7283/T5C53J2M	Delvaux, Damien, 2010, Africa Array GPS Network: ULUB-UNILU P.S., UNAVCO, GPS Data Set, doi:10.7283/T5C53J2M

Site Name	DOI	Reference
VWZM	10.7283/T5J38QW6	Nooner, Scott, Ebinger, Cynthia J., Saria, Elifuraha, Chindandali, Patrick, Ntambila, Daud, Shillington, Donna J., Pritchard, Matt, Elliott, Julie L., Nyblade, Andy, 2013, Malawi Rifting GPS Network, The GAGE Facility operated by UNAVCO, Inc., GPS/GNSS Observations (Aggregation of Multiple Datasets), https://doi.org/10.7283/T5J38QW6.
ZOMB	10.7283/T5BK19FQ	Nyblade, Andy, 2010, Africa Array GPS Network: ZOMB-Zomba P.S., UNAVCO, GPS Data Set, doi:10.7283/T5BK19FQ
ADIS	10.1007/s00190-008-0300-3	Dow, J.M., Neilan, R. E., and Rizos, C., The International GNSS Service in a changing landscape of Global Navigation Satellite Systems, Journal of Geodesy (2009) 83:191–198, DOI: 10.1007/s00190-008-0300-3
BRAZ		
CAS1		
DAKR		
DAV1		
DEAR		
DJIG		
FLRS		
FUNC		
GMAS		
GOUG		
HARB		
HNUS		
KERG		
KOUR		
LPAL		
MAL2		
MAS1		
MATE		
MAW1		
MAYG		
MFKG		
NIAM		
NKLG		
NOT1		
NURK		
OHI2		
OHI3		

Site Name	DOI	Reference
ONSA	10.1007/s00190-008-0300-3	Dow, J.M., Neilan, R. E., and Rizos, C., The International GNSS Service in a changing landscape of Global Navigation Satellite Systems, Journal of Geodesy (2009) 83:191–198, DOI: 10.1007/s00190-008-0300-3
PDEL		
POTS		
PRE1		
RAMO		
RBAY		
RCMN		
REUN		
SBOK		
SIMO		
SVTL		
SYOG		
TDOU		
VOIM		
WIND		
WSRT		
WUHN		
YIBL		

REFERENCES

Accardo, N. J., Gaherty, J. B., Shillington, D. J., Ebinger, C. J., Nyblade, A. A., Mbogoni, G. J., et al. (2017). Surface wave imaging of the weakly extended Malawi Rift from ambient-noise and teleseismic Rayleigh waves from onshore and lake-bottom seismometers. *Geophysical Journal International*, *209*(3), 1892–1905. https://doi.org/10.1093/gji/ggx133

Accardo, N. J., Shillington, D. J., Gaherty, J. B., Scholz, C. A., Nyblade, A. A., Chindandali, P. R. N., et al. (2018). Constraints on Rift Basin Structure and Border Fault Growth in the Northern Malawi Rift From 3-D Seismic Refraction Imaging. Journal of Geophysical Research: Solid Earth, 123(11), 10,003-10,025. https://doi.org/10.1029/2018JB016504

Ambraseys, N. N., & Adams, R. D. (1991). Reappraisal of Major African Earthquakes, South of 20°N, 1900-1930. Natural Hazards (Vol. 4).

Andersen, L. S., & Unrug, R. (1984). Geodynamic Evolution of the Bangweulu Block, Northern Zambia. Precambrian Research, 25, 187–212.

Argus, D. F., Gordon, R. G., Heflin, M. B., Ma, C., Eanes, R. J., Willis, P., et al. (2010). The angular velocities of the plates and the velocity of Earth's centre from space geodesy. Geophysical Journal International, 180(3), 913–960. https://doi.org/10.1111/j.1365-246X.2009.04463.x

Biggs, J., Nissen, E., Craig, T., Jackson, J., & Robinson, D. P. (2010). Breaking up the hanging wall of a rift-border fault: The 2009 Karonga earthquakes, Malawi. Geophysical Research Letters, 37(11). https://doi.org/10.1029/2010GL043179

Bird, P. (2003). An updated digital model of plate boundaries. Geochemistry, Geophysics, Geosystems, 4(3). https://doi.org/10.1029/2001GC000252

Bromage, T. G., Schrenk, F., & Juwayeyi, Y. M. (1995). Paleobiogeography of the Malawi Rift: Age and vertebrate paleontology of the Chiwondo Beds, northern Malawi. Journal of Human Evolution, 28(1), 37–57. https://doi.org/10.1006/jhev.1995.1005

Buck, W. R. (2004). Consequences of asthenospheric variability on continental rifting. Rheology and deformation of the lithosphere at continental margins, 62, 1–30.

Bulut, F., Bohnhoff, M., Eken, T., Janssen, C., Kl, T., & Dresen, G. (2012). The East Anatolian Fault Zone: Seismotectonic setting and spatiotemporal characteristics of seismicity based

on precise earthquake locations. Journal of Geophysical Research: Solid Earth, 117(7). https://doi.org/10.1029/2011JB008966

Calais, E., Ebinger, C. J., Hartnady, C., & Nocquet, J. M. (2006). Kinematics of the East African Rift from GPS and earthquake slip vector data. Geological Society Special Publication, 259, 9–22. https://doi.org/10.1144/GSL.SP.2006.259.01.03

Chorowicz, J. (2005). The East African rift system. Journal of African Earth Sciences, 43(1–3), 379–410. https://doi.org/10.1016/j.jafrearsci.2005.07.019

Contreras, J., Anders, M. H., & Scholz, C. H. (2000). Growth of a normal fault system: Observations from the Lake Malawi basin of the east African rift. Journal of Structural Geology, 22(2), 159–168. https://doi.org/10.1016/S0191-8141(99)00157-1

Craig, T. J., Jackson, J. A., Priestley, K., & Mckenzie, D. (2011). Earthquake distribution patterns in Africa: Their relationship to variations in lithospheric and geological structure, and their rheological implications. Geophysical Journal International, 185(1), 403–434. https://doi.org/10.1111/j.1365-246X.2011.04950.x

Daly, M. C. (1986). Crustal shear zones and thrust belts: their geometry and continuity in Central Africa. Philosophical Transactions of the Royal Society of London. Series A, Mathematical and Physical Sciences, 317(1539), 111–128. https://doi.org/10.1098/rsta.1986.0028

Delvaux, D., & Barth, A. (2010). African stress pattern from formal inversion of focal mechanism data. Tectonophysics, 482(1–4), 105–128. https://doi.org/10.1016/j.tecto.2009.05.009

Delvaux, D. (2001). Karoo rifting in western Tanzania: precursor of Gondwana break-up? Tectonics of the Ardenne Allochtonn in the North Variscan Front View project Seismotectonic Map of Africa IGCP 601 View project Karoo rifting in western Tanzania: precursor of Gondwana break-up? Retrieved from https://www.researchgate.net/publication/268303813

Delvaux, D., Levi, K., Kajara, R., Sarota Delvaux, J., Delvaux, D., Levi, K., et al. (1992). Cenozoic paleostress and kinematic evolution of the Rukwa-North Malawi rift valley (East African Rift System). Bull Centres Recti. Explor-Prod. Elf Aquitaine, 16, 383–406. Retrieved from https://www.researchgate.net/publication/278441906

Déprez, A., Doubre, C., Masson, F., & Ulrich, P. (2013). Seismic and aseismic deformation along the East African Rift System from a reanalysis of the GPS velocity field of Africa.

Geophysical Journal International Geophys. J. Int, 193(3), 1353–1369. https://doi.org/10.1093/gji/ggt085ï

Domingues, A., Silveira, G., Ferreira, A. M. G., Chang, S. J., Custodio, S., & Fonseca, J. F. B. D. (2016). Ambient noise tomography of the East African Rift in Mozambique. Geophysical Journal International, 204(3), 1565–1578. https://doi.org/10.1093/gji/ggv538

Ebinger, C. J. (1989a). Geometric and Kinematic Development of Border Faults and Accommodation Zones, Kivu-Rusizi Rift, Africa. TECTONICS, 8(1), 117–133.

Ebinger, C. J. (1989b). Tectonic development of the western branch of the East African rift system. Geological Society of America Bulletin, 101, 885–903. Retrieved from https://pubs.geoscienceworld.org/gsa/gsabulletin/article-pdf/101/7/885/3380526/i0016-7606-101-7-885.pdf

Ebinger, C. J., & Sleep, N. (1998). Cenozoic magmatism throughout East Africa resulting from impact of a single plume. Nature 395, 788–791 (1998). Nature, (395), 788–791.

Ebinger, C. J., Crow, M. J., Rosendahl, B. R., Livingstone, D. A., & Lefournier, J. (1984). Structural evolution of Lake Malaŵi, Africa. Nature, 308(5960), 627–629. https://doi.org/10.1038/308627a0

Ebinger, C. J., Rosendahl, B. R., & Reynolds, D. J. (1987). Tectonic model of the Malawi rift, Africa. Tectonophysics, 141, 215–235.

Ebinger, C. J., Deino, A. L., Tesha, A. L., Becker, T., & Ring, U. (1993). Tectonic controls on rift basin morphology: evolution of the northern Malawi (Nyasa) Rift. Journal of Geophysical Research, 98(B10), 17821–17836. https://doi.org/10.1029/93jb01392

Ebinger, C. J., Oliva, S. J., Pham, T. Q., Peterson, K., Chindandali, P., Illsley-Kemp, F., et al. (2019). Kinematics of Active Deformation in the Malawi Rift and Rungwe Volcanic Province, Africa. Geochemistry, Geophysics, Geosystems, 20(8), 3928–3951. https://doi.org/10.1029/2019GC008354

Elliott, J. L., Larsen, C. F., Freymueller, J. T., & Motyka, R. J. (2010). Tectonic block motion and glacial isostatic adjustment in southeast Alaska and adjacent Canada constrained by GPS measurements. Journal of Geophysical Research: Solid Earth, 115(9). https://doi.org/10.1029/2009JB007139

Engdahl, E. R., di Giacomo, D., Sakarya, B., Gkarlaouni, C. G., Harris, J., & Storchak, D. A. (2020). ISC-EHB 1964–2016, an Improved Data Set for Studies of Earth Structure and Global Seismicity. Earth and Space Science, 7(1). https://doi.org/10.1029/2019EA000897

Engdahl, E. R., van der Hilst, R., & Buland, R. (1998). Global Teleseismic Earthquake Relocation with Improved Travel Times and Procedures for Depth Determination. Bulletin of the Seismological Society of America (Vol. 88).

Fernandes, R. M. S., Ambrosius, B. A. C., Noomen, R., Bastos, L., Combrinck, L., Miranda, J. M., & Spakman, W. (2004). Angular velocities of Nubia and Somalia from continuous GPS data: Implications on present-day relative kinematics. Earth and Planetary Science Letters, 222(1), 197–208. https://doi.org/10.1016/j.epsl.2004.02.008

Flannery, J. W., & Rosendahl, B. R. (1990). The seismic stratigraphy of Lake Malawi, Africa: implications for interpreting geological processes in lacustrine rifts. Journal of African Earth Sctences (Vol. 10).

Flesch, L. M., Holt, W. E., Haines, A. J., & Shen-Tu, B. (2000). Dynamics of the Pacific-North American Plate Boundary in the Western United States. Science, 287(5454), 834–836. Retrieved from http://science.sciencemag.org/

Franke, D., Jokat, W., Ladage, S., Stollhofen, H., Klimke, J., Lutz, R., et al. (2015). The offshore East African Rift System: Structural framework at the toe of a juvenile rift. Tectonics, 34(10), 2086–2104. https://doi.org/10.1002/2015TC003922

Fu, Y., & Freymueller, J. T. (2012). Seasonal and long-term vertical deformation in the Nepal Himalaya constrained by GPS and GRACE measurements. Journal of Geophysical Research: Solid Earth, 117(3). https://doi.org/10.1029/2011JB008925

Fu, Y., Freymueller, J. T., & van Dam, T. (2012). The effect of using inconsistent ocean tidal loading models on GPS coordinate solutions. Journal of Geodesy, 86(6), 409–421. https://doi.org/10.1007/s00190-011-0528-1

Gaherty, J. B., Zheng, W., Shillington, D. J., Pritchard, M. E., Henderson, S. T., Chindandali, P. R. N., et al. (2019). Faulting processes during early-stage rifting: Seismic and geodetic analysis of the 2009-2010 Northern Malawi earthquake sequence. Geophysical Journal International, 217(3), 1767–1782. https://doi.org/10.1093/gji/ggz119

Gupta, H. K., & Malomo, S. (1995). The Malawi earthquake of March 10, 1989: report of field survey. Seismological Research Letters, 66(1), 20–27. https://doi.org/10.1785/gssrl.66.1.20

Halldórsson, S. A., Hilton, D. R., Scarsi, P., Abebe, T., & Hopp, J. (2014). A common mantle plume source beneath the entire East African Rift System revealed by coupled helium-neon systematics. Geophysical Research Letters, 41(7), 2304–2311. https://doi.org/10.1002/2014GL059424

Hansen, S. E., & Nyblade, A. A. (2013). The deep seismic structure of the Ethiopia/Afar hotspot and the African superplume. Geophysical Journal International, 194(1), 118–124. https://doi.org/10.1093/gji/ggt116

Heilman, E., Kolawole, F., Atekwana, E. A., & Mayle, M. (2019). Controls of Basement Fabric on the Linkage of Rift Segments. Tectonics, 38(4), 1337–1366. https://doi.org/10.1029/2018TC005362

Hodge, M., Biggs, J., Goda, K., & Aspinall, W. (2015). Assessing infrequent large earthquakes using geomorphology and geodesy: the Malawi Rift. Natural Hazards, 76(3), 1781–1806. https://doi.org/10.1007/s11069-014-1572-y

Holt, W. E., Chamot-Rooke, N., le Pichon, X., Haines, A. J., Shen-Tu, B., & Ren, J. (2000). Velocity field in Asia inferred from Quaternary fault slip rates and Global Positioning System observations. Journal of Geophysical Research: Solid Earth, 105(B8), 19185–19209. https://doi.org/10.1029/2000jb900045

Horner-Johnson, B. C., Gordon, R. G., Cowles, S. M., & Argus, D. F. (2005). The angular velocity of Nubia relative to Somalia and the location of the Nubia-Somalia-Antarctica triple junction. Geophysical Journal International, 162(1), 221–238. https://doi.org/10.1111/j.1365-246X.2005.02608.x

Horner-Johnson, B. C., Gordon, R. G., & Argus, D. F. (2007). Plate kinematic evidence for the existence of a distinct plate between the Nubian and Somalian plates along the Southwest Indian Ridge. Journal of Geophysical Research: Solid Earth, 112(5). https://doi.org/10.1029/2006JB004519

International Seismological Centre. (2020). ISC-EHB Dataset. https://doi.org/https://doi.org/10.31905/PY08W6S3

Jackson, M., & Blenkinsop, T. (1997). The Bilila-Mtakataka fault in Malawi: An active, 100-km long, normal fault segment in thick seismogenic crust. Tectonics, 16(1), 137–150. https://doi.org/10.1029/96TC02494

Jestin, F., Huchon, P., & Gaulier, J. M. (1994). The Somalia plate and the East African Rift System: present-day kinematics. Geophysical Journal International, 116(3), 637–654. https://doi.org/10.1111/j.1365-246X.1994.tb03286.x

Kolawole, F., Atekwana, E. A., Laó-Dávila, D. A., Abdelsalam, M. G., Chindandali, P. R., Salima, J., & Kalindekafe, L. (2018). Active Deformation of Malawi Rift's North Basin Hinge Zone Modulated by Reactivation of Preexisting Precambrian Shear Zone Fabric. Tectonics, 37(3), 683–704. https://doi.org/10.1002/2017TC004628

Laõ-Dávila, D. A., Al-Salmi, H. S., Abdelsalam, M. G., & Atekwana, E. A. (2015). Hierarchical segmentation of the Malawi Rift: The influence of inherited lithospheric heterogeneity and kinematics in the evolution of continental rifts. Tectonics, 34(12), 2399–2417. https://doi.org/10.1002/2015TC003953

Lavayssière, A., Drooff, C., Ebinger, C., Gallacher, R., Illsley-Kemp, F., Oliva, S. J., & Keir, D. (2019). Depth Extent and Kinematics of Faulting in the Southern Tanganyika Rift, Africa. Tectonics, 38(3), 842–862. https://doi.org/10.1029/2018TC005379

Le Gall, B., Gernigon, L., Rolet, J., Ebinger, C., Gloaguen, R., Nilsen, O., et al. (2004). Neogene-Holocene rift propagation in central Tanzania: Morphostructural and aeromagnetic evidence from the Kilombero area. Bulletin of the Geological Society of America, 116(3–4), 490–510. https://doi.org/10.1130/B25202.1

Lemna, O. S., Stephenson, R., & Cornwell, D. G. (2019). The role of pre-existing Precambrian structures in the development of Rukwa Rift Basin, southwest Tanzania. Journal of African Earth Sciences, 150, 607–625. https://doi.org/10.1016/j.jafrearsci.2018.09.015

Lloyd, R., Biggs, J., & Copley, A. (2019). The decade-long Machaze-Zinave aftershock sequence in the slowly straining Mozambique Rift. Geophysical Journal International, 217(1), 504–531. https://doi.org/10.1093/gji/ggz033

Loveless, J. P., & Meade, B. J. (2010). Geodetic imaging of plate motions, slip rates, and partitioning of deformation in Japan. Journal of Geophysical Research, 115(B2). https://doi.org/10.1029/2008jb006248

Macgregor, D. (2015, January 1). History of the development of the East African Rift System: A series of interpreted maps through time. Journal of African Earth Sciences. Elsevier Ltd. https://doi.org/10.1016/j.jafrearsci.2014.09.016

McCaffrey, R. (2002), Crustal block rotations and plate coupling, in Plate Boundary Zones, Geodynamics Series, vol. 30, edited by S. Stein and J. Freymueller, pp. 101–122, AGU, Washington, D. C.

McCartney, T., & Scholz, C. A. (2016). A 1.3 million year record of synchronous faulting in the hangingwall and border fault of a half-graben in the Malawi (Nyasa) Rift. Journal of Structural Geology, 91, 114–129. https://doi.org/10.1016/j.jsg.2016.08.012

McConnell, R. B. (1972). Geological Development of the Rift System of Eastern Africa. GSA Bulletin, 83(9), 2549–2572. https://doi.org/10.1130/0016-7606(1972)83[2549:gdotrs]2.0.co;2

Meade, B. J., & Hager, B. H. (2005). Block models of crustal motion in southern California constrained by GPS measurements. Journal of Geophysical Research: Solid Earth, 110(3), 1–19. https://doi.org/10.1029/2004JB003209

Meade, B. J., & Loveless, J. P. (2009). Block modeling with connected fault-network geometries and a linear elastic coupling estimator in spherical coordinates. Bulletin of the Seismological Society of America, 99(6), 3124–3139. https://doi.org/10.1785/0120090088

Mortimer, E., Paton, D. A., Scholz, C. A., Strecker, M. R., & Blisniuk, P. (2007). Orthogonal to oblique rifting: Effect of rift basin orientation in the evolution of the North basin, Malawi Rift, East Africa. Basin Research, 19(3), 393–407. https://doi.org/10.1111/j.1365-2117.2007.00332.x

Mulibo, G. D., & Nyblade, A. A. (2016). The seismotectonics of Southeastern Tanzania: Implications for the propagation of the eastern branch of the East African Rift. Tectonophysics, 674, 20–30. https://doi.org/10.1016/j.tecto.2016.02.009

Njinju, E. A., Kolawole, F., Atekwana, E. A., Stamps, D. S., Atekwana, E. A., Abdelsalam, M. G., & Mickus, K. L. (2019). Terrestrial heat flow in the Malawi Rifted Zone, East Africa: Implications for tectono-thermal inheritance in continental rift basins. Journal of Volcanology and Geothermal Research, 387. https://doi.org/10.1016/j.jvolgeores.2019.07.023

O'Donnell, J. P., Adams, A., Nyblade, A. A., Mulibo, G. D., & Tugume, F. (2013). The uppermost mantle shear wave velocity structure of eastern africa from rayleigh wave tomography: Constraints on rift evolution. Geophysical Journal International, 194(2), 961–978. https://doi.org/10.1093/gji/ggt135

O'Donnell, J. P., Selway, K., Nyblade, A. A., Brazier, R. A., el Tahir, N., & Durrheim, R. J. (2016). Thick lithosphere, deep crustal earthquakes and no melt: A triple challenge to understanding extension in the western branch of the East African Rift. Geophysical Journal International, 204(2), 985–998. https://doi.org/10.1093/gji/ggv492

Okada, Y. (1985). Surface deformation due to shear and tensile faults in a half-space. Bulletin of the Seismological Society of America, 75(4), 1135–1154.

Reilinger, R., & McClusky, S. (2011). Nubia-Arabia-Eurasia plate motions and the dynamics of Mediterranean and Middle East tectonics. Geophysical Journal International, 186(3), 971–979. https://doi.org/10.1111/j.1365-246X.2011.05133.x

Ring, U., & Betzler, C. (1995). Geology of the Malawi Rift: Kinematic and tectonosedimentary background to the Chiwondo Beds, northern Malawi. Journal of Human Evolution, 28(1), 7–21. https://doi.org/10.1006/jhev.1995.1003

Roberts, E. M., Stevens, N. J., O'Connor, P. M., Dirks, P. H. G. M., Gottfried, M. D., Clyde, W. C., et al. (2012). Initiation of the western branch of the East African Rift coeval with the eastern branch. Nature Geoscience, 5(4), 289–294. https://doi.org/10.1038/ngeo1432

Rosendahl, B. R., Kilembe, E., & Kaczmarick, K. (1992). Comparison of the Tanganyika, Malawi, Rukwa and Turkana Rift zones from analyses of seismic reflection data. Tectonophysics, 213, 235–256.

Saria, E., Calais, E., Altamimi, Z., Willis, P., & Farah, H. (2013). A new velocity field for Africa from combined GPS and DORIS space geodetic Solutions: Contribution to the definition of the African reference frame (AFREF). Journal of Geophysical Research: Solid Earth, 118(4), 1677–1697. https://doi.org/10.1002/jgrb.50137

Saria, E., Calais, E., Stamps, D. S., Delvaux, D., & Hartnady, C. J. H. (2014). Present-day kinematics of the East African Rift. Journal of Geophysical Research: Solid Earth, 119(4), 3584–3600. https://doi.org/10.1002/2013JB010901

Scholz, C. A., Rosendahl, B. R., Versfelt, J. W., Kaczmarick, K. J., Schwede, W., & Woods, L. D. (1989). Seismic Atlas of Lake Malawi (Nyasa), East Africa. Project PROBE, Geology Dept., Duke University, Durham, NC.

Sella, G. F., Dixon, T. H., & Mao, A. (2002). REVEL: A model for Recent plate velocities from space geodesy. Journal of Geophysical Research: Solid Earth, 107(B4), ETG 11-1-ETG 11-30. https://doi.org/10.1029/2000jb000033

Shillington, D. J., Gaherty, J. B., Ebinger, C. J., Scholz, C. A., Selway, K., Nyblade, A. A., et al. (2016). Acquisition of a unique onshore/offshore geophysical and geochemical dataset in the northern Malawi (Nyasa) rift. Seismological Research Letters, 87(6), 1406–1416. https://doi.org/10.1785/0220160112

Shillington, D. J., Scholz, C. A., Chindandali, P. R. N., Gaherty, J. B., Accardo, N. J., Onyango, E., et al. (2020). Controls on rift faulting in the North Basin of the Malawi (Nyasa) Rift, East Africa. Tectonics. https://doi.org/10.1029/2019tc005633

Specht, T. D., & Rosendahl, B. R. (1989). Architecture of the Lake Malawi Rift, East Africa. Journal of African Earth Sciences (Vol. 8).

Stamps, D. S., Calais, E., Saria, E., Hartnady, C., Nocquet, J. M., Ebinger, C. J., & Fernandes, R. M. (2008). A kinematic model for the East African Rift. Geophysical Research Letters, 35(5). https://doi.org/10.1029/2007GL032781

Stamps, D. S., Saria, E., & Kreemer, C. (2018). A Geodetic Strain Rate Model for the East African Rift System. Scientific Reports, 8(1). https://doi.org/10.1038/s41598-017-19097-w

U.S. Department of the Interior U.S. Geological Survey. (2018). M 5.5-24 km NE of Nsanje, Malawi (available at https://earthquake.usgs.gov/earthquakes/eventpage/us1000d1cy#executive, last accessed 21 Oct 2019).

Weston, J., Engdahl, E. R., Harris, J., di Giacomo, D., & Storchak, D. A. (2018). ISC-EHB: Reconstruction of a robust earthquake data set. Geophysical Journal International, 214(1), 474–484. https://doi.org/10.1093/gji/ggy155

Williams, J. N., Fagereng, Å., Wedmore, L. N. J., Biggs, J., Mphepo, F., Dulanya, Z., et al. (2019). How Do Variably Striking Faults Reactivate During Rifting? Insights From Southern Malawi. Geochemistry, Geophysics, Geosystems, 20(7), 3588–3607. https://doi.org/10.1029/2019GC008219